Detection of movement of hemozoin crystals in the digestive vacuole of malaria parasites

Vanessa Alexandra Magalhães Costa

Thesis to obtain the Master in

Biomedical Technologies

Supervisors: Professor Patrícia Maria Cristovam Cipriano Almeida de Carvalho and
Doctor Maria de Fátima Carvalho Nogueira

Examination Committee

Chairperson: Professor Raúl Daniel Lavado Carneiro Martins
Supervisor: Professor Patrícia Maria Cristovam Cipriano Almeida de Carvalho
Members of the committee: Professor João Manuel Melo de Sousa

December 2014

Acknowledgments

Aproveito este espaço para agradecer a todas as pessoas que me ajudaram a cumprir os meus objectivos e a realizar mais esta etapa da minha formação académica. Desta forma, manifesto a minha gratidão através de algumas palavras.

À minha orientadora **Professora Patrícia Maria Cristovam Cipriano Almeida de Carvalho**, pela forma como me orientou, pelo entusiasmo e motivação. É importante referir ainda a disponibilidade incansável manifestada, apesar do seu horário demasiado preenchido, o seu apoio incondicional e confiança. Muito obrigada por tudo, Professora.

Ao **Sérgio Gonçalves (IST)** pela paciência, pelo tempo despendido, pela total disponibilidade e por me ter ensinado tanto. És um grande amigo.

À **Marta Machado (IHMT)** pela amizade demonstrada ao longo deste trabalho, pela vontade de me ajudar e pela disponibilidade manifestada.

A **Doutora Maria de Fátima Carvalho Nogueira** pela paciência, pelo apoio e por toda a disponibilidade manifestada que me ajudou a concluir este trabalho.

Aos meus **Pais**, por terem acreditado em mim e me terem dado oportunidade de concluir mais uma etapa muito importante na minha vida.

Obrigada por tudo.

Abstract

Malaria results from protozoan infection of red blood cells by four species of *Plasmodium*, of which *falciparum* is the worst. In the intra-erythocytic cycle the parasite evolves through three stages: ring, trophozoite and schizont. The digestion of hemoglobin releases high quantities of toxic heme, which the parasite crystallizes into hemozoin in the digestive vacuole. This crystallization is a dynamic process, which is poorly understood. The analysis of the crystals' movement is the focus of this work. The hemozoin movement in the digestive vacuole of parasites in trophozoite stage was studied at room temperature after culturing at 37°C and after exposure to 40°C and 41°C for 1 hour through real-time microscopy using a high-speed camera coupled to an optical microscope. MegaSpeed and FastCam cameras were used to acquire image sequences at 2128, 4000, 7500 and 15000 fps. The frames were analyzed using scripts developed in ImageJ and Matlab. The average projected displacement of the particles is 0.236±0.090 μm (2128 fps) and 0.190±0.083 μm (4000 fps) and the average velocity is 52.5±21.3 μm/s (2128 fps) and 64.7±25.2 μm/s (4000 fps). The exposure to febrile temperatures dampened the hemozoin movement. However, the hemozoin movement partially resumed after 1 hour at room temperature for the heat treatment at 40°C. This demonstrates that the phenomenon is not Brownian. The apparently high driving force involved in this activity suggests that the phenomenon plays a vital role and that forced immobilization may lead to parasite destruction and innovative therapies.

Keywords: Malaria, hemozoin, movement, velocity, temperature, digestive vacuole

Resumo

A malária resulta da infecção protozoária das células vermelhas do sangue por quatro espécies de *Plasmodium*, onde *falciparum* é a pior. No ciclo intra-eritrócito o parasita passa por três fases: anel, trofozoíto e esquizonte. A digestão da hemoglobina liberta grandes quantidades de heme tóxico, que o parasita cristaliza em hemozoína no vacúolo digestivo. Esta cristalização é um processo dinâmico, que está pouco compreendido. A análise do movimento dos cristais à temperatura corporal saudável e após exposição a febre é o foco deste trabalho. O movimento da hemozoína no vacúolo digestivo de parasitas no estágio trofozoíto foi estudado a temperatura ambiente após cultura a 37°C e depois da exposição a 40°C e 41ºC durante 1 hora, através de microscopia em tempo real utilizando uma câmara de alta velocidade acoplada a um microscópio óptico. Utilizaram-se as câmaras MegaSpeed e Fastcam para adquirir as sequências de imagens a 2128, 4000, 7500 e 15000 fps. As frames foram analisadas utilizando scripts desenvolvidos para ImageJ e Matlab. O deslocamento projetado médio das partículas 0.236±0.090 µm (2128 fps) e 0.190±0.083 µm (4000 fps) e a velocidade média é 52.5±21.3 µm/s (2128 fps) e 64.7±25.2 µm/s (4000 fps). A exposição a febre atenuou o movimento da hemozoína. No entanto, o movimento retoma parcialmente após 1 hora à temperatura ambiente, durante o tratamento térmico a 40°C. Isto demonstra que o fenómeno não é Browniano. A alta força motriz aparentemente envolvida nesta atividade sugere que o fenómeno tem um papel vital e que a imobilização forçada pode levar à destruição do parasita e terapias inovadoras.

Palavras-chave: Malária, hemozoína, movimento, velocidade, temperatura, vacúolo digestivo

Geral Index

Figures Index

Tables Index

List of abbreviations used throughout the text

P. falciparum – *Plasmodium falciparum*

RBC - Red blood cells

Hb - Hemoglobin (Hb)

HZ - Hemozoin (malaria pigment)

DV - Digestive vacuole

iRBC - Infected red blood cells

SP - Sulfadoxine-pyrimethamine

ACT - Artemisinin-based combination

IMM - Institute of Molecular Medicine

IHMT - Instituto de Higiene e Medicina Tropical

1. Introduction

Malaria is known as one of the most common and lethal parasitic infections in the world. About 40% of the world's population lives in malaria-endemic areas and this disease is responsible for up to 500 million episodes of clinical infection and 2.7 million deaths every year. It is estimated that in 2012 malaria caused 627 000 deaths mostly among African children [1, 12].

Malaria is found all over the tropical and subtropical regions of the world (see figure 1). The intensity and the pattern of transmission of malaria may differ noticeably within the same country as a result of variations in altitude or rainfall, social and environmental factors, coverage of health services and malaria control activities [2].
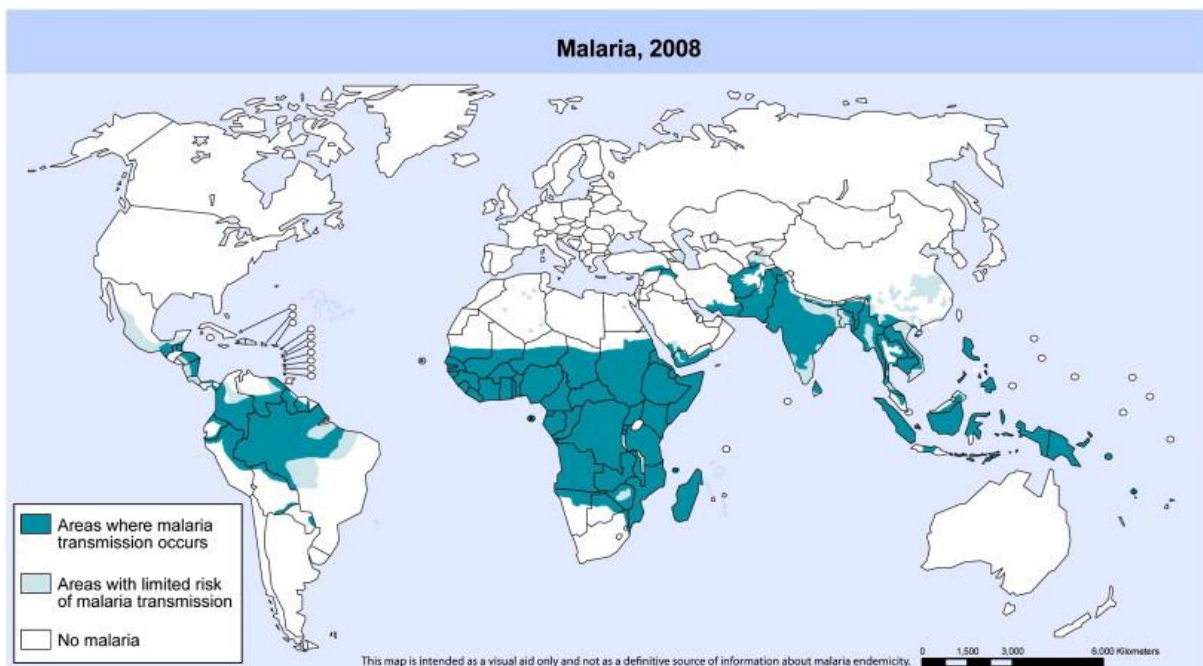
Figure 1 – Global malaria distribution [3].

Malaria results from a protozoan infection of red blood cells caused in humans by four species of the genus *Plasmodium*, of which *falciparum* is the worst, while the other species that induce malaria are rarely deathly or responsible for persistent squeals. The transmission results exclusively through the bite of an infected female anopheline mosquito [1, 2].

Malaria typically presents symptoms of a nonspecific flu-like illness, with fever (every 48–72 hours), chills, headache, muscle aches, nausea, anorexia, and fatigue. The severity and course of an attack is related to the species and strain of the infecting parasite, as well as the age, genetic constitution, malaria-specific immunity, general health, and nutritional status of the patient, and on previous antimalarial drug use. The clinical condition of a nonimmune person with *falciparum* malaria who is untreated or in whom effective antimalarial treatment is delayed will deteriorate quickly, probably resulting in severe disease and death [2].

To discuss the challenges connected to malaria therapy, the complexity of the disease should be taken into consideration and the biological aspects of the parasite at different stages of its development in infected humans must be understood. The life cycle of malaria (see figures 2 and 3) in a human host begins when the infected mosquito bites the person. The inoculated sporozoites migrate to the liver and invade the hepatocytes by mechanisms not entirely understood. Each sporozoite generates thousands of new parasites that are released into the bloodstream as merozoites, an invasive form fit to start the asexual blood stages in red blood cells (RBC), known as the intra-erythrocytic cycle. After invasion the parasite stays relatively inactive metabolically for 10–15 hours (the ring stage); then begins to ingest and digest hemoglobin (Hb) as it matures to trophozoite (a phase of rapid growth over the next 25 hours). In the final schizont stage the parasite digests the greater part of the hemoglobin and grows to fill more than 50% of the volume of the host cells, dividing into thousands merozoites that 48 hours after invasion lyse the RBC to be released into the bloodstream, restarting a new cycle. In most of the intra-erythrocytic cycle the parasite remains relatively hidden in the host cells and malaria is asymptomatic. However, exposure to the host immune system at the invasion stage turns the released merozoites into the principal etiological agents of malaria, causing the classical symptoms of the disease to manifest around two weeks after the mosquito-vectored sporozoite inoculation. During the intra-erythrocytic cycle the *P. falciparum* parasite consumes up to 80% of the host cell hemoglobin [27]. The digestion of hemoglobin releases high quantities of heme (a toxic compound lethal to the parasite) which the parasite crystallizes into paramagnetic hemozoin crystals (malaria pigment) (HZ) in its digestive vacuole (DV) [28]. Polymerization of heme into HZ is unique to hematophagous organisms like malaria parasites and has been a preferential target for antimalarial drug design. Pathological studies of the malaria's intra-erythrocytic cycle show that severe modifications occur in the infected red blood cells (iRBC), including (i) an order-of-magnitude increase in cell stiffness related with a clearly diminished deformability and (ii) formation of adhesive "knobs" at the iRBC surface (which are electron-dense nanoscale protrusions on the surface of *P. falciparum*-iRBC) that allow cytoadherence to endothelial cells at the internal walls of blood vessels. Cytoadherence prevents mature iRBCs from reaching the spleen, where they would be cleared from the bloodstream due to their reduced deformability [3-6, 8-11]. However, the resulting microvascular obstruction leads to vital organ dysfunction, particularly in the brain and placenta, leading respectively to cerebral and placental malaria, which are often fatal.
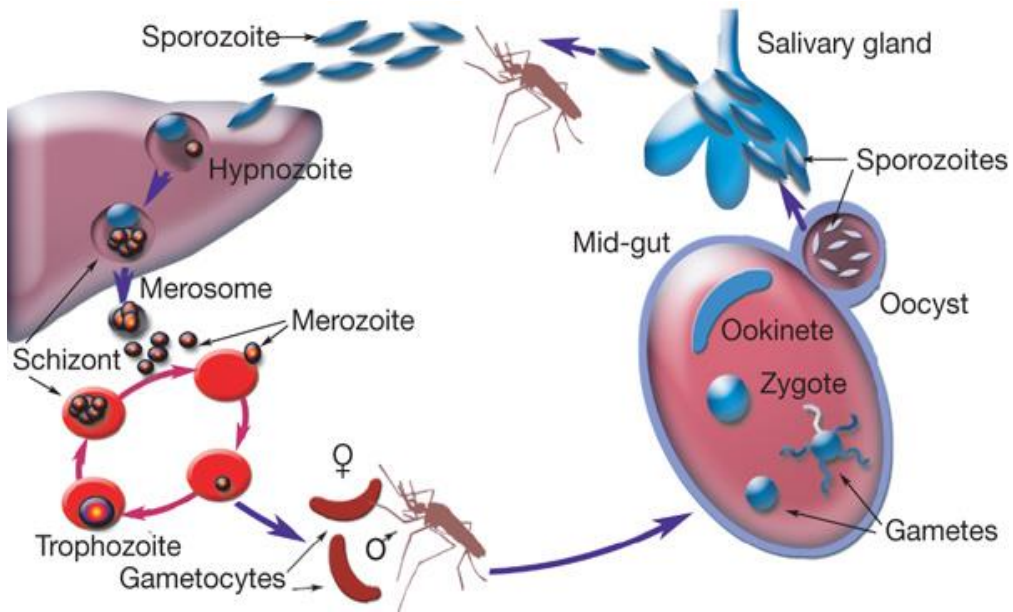
Figure 2 – Life cycle of malaria [13].
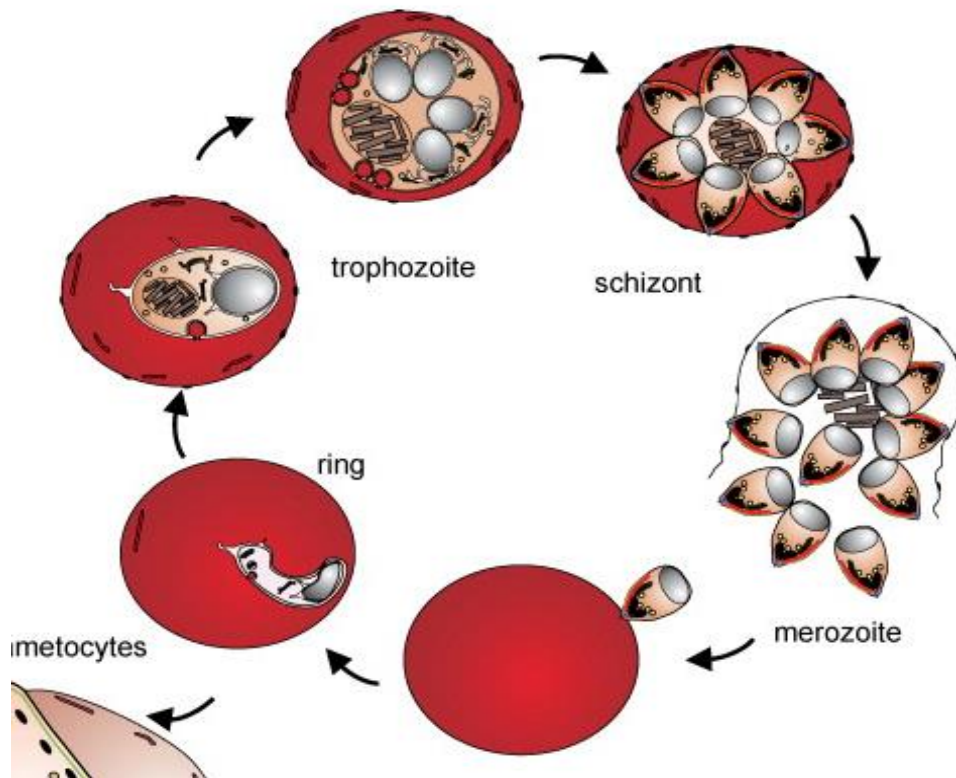
Figure 3 – The intra-erythrocytic cycle [16].

There have been enormous advances in the understanding of disease mechanisms since the first description of malarial parasites by Laveran in 1880 [1]. These advances have resulted from exhaustive studies in patients, animal models of infection, biochemical, cellular, and molecular investigations; and have enhanced our comprehension of the disease processes, although there are still no therapies fully successful in avoiding mortality from severe infection. Preventing or treating malaria parasite infections in the human host depends heavily on chemoprophylaxis and chemotherapy, due to the continued absence of clinically proven vaccines (altogether, 27 vaccines reached clinical trials in humans [12, 17, 18], although none has yet been licensed by health organizations). Antimalarials interfere essentially with hemoglobin digestion, although the mechanisms are still not completely understood. Early in the XX century, the widespread application of efficient insecticides and antimalarial drugs led to a decline in the incidence of malaria, and some countries were rendered malaria free. However, resistance to antimalarial medicines is a recurring problem. In the 1970s and 1980s, insecticides failed to curb transmission by anopheline mosquitoes and global resistance to chloroquine and sulfadoxine-pyrimethamine (SP) (the cheapest formulations) emerged. As a result, the incidence of malaria increased and the disease became more and more widespread, undermining malaria control efforts. Artemisinin-based combination therapies (ACT) are currently a highly efficacious line of antimalarials. However, the border area between Cambodia and Thailand has been since the 1970s the epicenter of emerging malaria drug resistance, which started with resistance to chloroquine, followed by resistance to sulfadoxine-pyrimethamine, and currently there is already an increasing failure rate in treating *Plasmodium falciparum* infection with ACT [1, 12, 14, 15]. Globally, the resistance of the malaria parasite, especially of *P. falciparum*, to commonly recommended antimalarial drugs has become one of the greatest challenges in malaria control and the complexity of the parasite life cycle is the primary factor behind the lack of alternative therapeutics [1, 2, 4, 21].

A better understanding of the pathophysiological processes of malaria is required in order to reduce the mortality and morbidity of the disease. Therefore, research efforts are necessary to provide prompt and accurate diagnosis and effective treatment, principally to the rural low-income populations who are severely affected by malaria [2]. Most investigations have their focus on the biochemical mechanisms of hemoglobin digestion in acidic digestive vacuole of *P. falciparum* [8], which have important implications for the complex host-parasite inter-relationship and also for the mode of action of several of the most effective antimalarial drugs. However, in view of the decreased sensitivity for artemisinin–based therapies that essentially interfere with hemoglobin digestion novel treatment strategies are on demand.

The observation with real-time optical microscopy of viable parasites in late development stages showed that HZ crystals move in the parasite's digestive vacuole at a significantly high speed [9-11]. Sachanonta et al reported the effects of quinine, piperaquine and artesunate on parasitemia, on parasite stage development and on *P. falciparum* morphology using real-time light microscopy or Transmission Electron Microscopy (TEM) in order to identify the ultrastructural changes associated with drug-treatment [10]. Only artemisinin-treated iRBC showed a significant difference from controls in loss of hemozoin movement in the trophozoite. The development stage was significantly retarded, with reduction of parasite's size, pyknotic changes and death in direct proportion to exposure time. In

addition, the digestive vacuoles were rare and quite small with limited hemozoin crystals formation and exhibited complete disorganization. The loss of hemozoin movement can be one of the first indicators of an adverse parasite response to external stimuli, before distinct morphological changes occur [10]. Wongtanachai et al reported the effects antimalarial drugs on movement of *P. falciparum* with similar results and proposed that the random movement of pigment crystals is of Brownian nature - greater pigments have slower movement - and that the movement of parasites was determined by movement of hemozoin within the digestive vacuole of the parasite [11]. Biagini et al also investigated the digestive vacuole of the malaria parasite using real-time microscopy and concluded that this digestive vacuole is a dynamic intracellular Ca2+ store [8].

Since the crystals are paramagnetic [7], the application of magnetic fields may be a potential new therapeutic approach since hampering their motion may decrease the parasite survival chances. Recently, Butykai et al described the dynamics of the magnetically driven rotation of HZ crystals in fluids with different viscosity such as water, acetone, hemolyzed blood, etc. These findings may be relevant not only in malaria diagnosis and therapies, where hemozoin is considered as drug target or immune modulator, but also in the magnetic manipulation of cells at the microscopic scale [7].

However, only a mechanical characterization of the hemozoin movement will allow a quantitative analysis of the effect of drugs on crystal motion as well as establishing a quantitative correlation between drug-induced or magnetically-induced damping and parasite viability.

2. Objectives

2.1. Geral objetives

In viable parasites the hemozoin crystals move in the parasite vacuole [9-11] and this dynamic process of crystal growth, which to the best of my knowledge has not been investigated, may represent the means for an efficient collection of crystallizing units and the phenomenon calls for renovated attention. The apparently high driving force involved in this activity suggests that the phenomenon plays a vital role and that forced immobilization may lead to parasite destruction. The movement of hemozoin crystals and its possible damping by physical/chemical means, needs to be addressed from an engineering perspective and elucidating the details of the dynamic behavior of hemozoin crystals constitutes the purpose of the present work. The study of HZ movement may provide an innovative approach for parasite elimination and this preliminary investigation may raise interest on the potential of transforming HZ movement into a target for innovative therapies.

2.2. Specific objective

The movement of hemozoin crystals in the digestive vacuole of parasites in late trophozoite stage was studied by real-time microscopy (RTM) using a video camera coupled to an optical microscope. Parasites of the 3D7 and 2D2 strains were used in the investigations. The study aims to characterize the dynamic behavior of hemozoin crystals cultured at healthy body temperature and after exposure to febrile temperatures. The higher temperature is expected to stall the crystal movement and the possible resuming of movement will also be evaluated.

3. Materials and methods

3.1. Cultures

The *Plasmodium falciparum* species was selected for the investigation, as it is the deadliest of the malaria parasites and the only that can be maintained in culture. As mentioned above, there are dozens of strains of *P. falciparum* resistant and susceptible to different types of drugs (see table 1). The strains investigated were the well-known 3D7 (susceptible to chloroquine and mefloquine) and DD2 (resistant to chloroquine and mefloquine). The 3D7 is the "type strain" of *P. falciparum* used as a basis to total genome sequencing which is deposited on PlasmoDB (http://plasmodb.org/plasmo/). Only late stage trophozoites were studied to better observe the hemozoin changes.

The parasite cultivation followed the following protocol: *P. falciparum* 3D7 and DD2 strains were continuously cultured and synchronized as previously described by Trager and Jensen (1976) [25], with minor modifications. Briefly, parasites were cultivated on human erythrocytes suspended in RPMI 1640 medium supplemented with HEPES, hypoxanthine and 10% AlbuMAX II, at pH 7.2. Cultures were maintained at 37ºC under an atmosphere of 5% CO_2 and synchronized by sorbitol treatment (Lambros and Vanderberg, 1979) [26] prior to the experiments. Stages and parasitaemia were determined by light microscopy observation of Giemsa-stained thin blood smears. These cultures were cultured at Instituto de Higiene e Medicina Tropical (IHMT) and the infected red blood cells were brought to IST under controlled temperature conditions for the measurements.

			Phenotype	
Clone	Origin	Reference	S	R
HB3	Honduras	(Bhasin & Trager, 1984)	CQ, Mef and QN	-
3D7	?	(Rosario, 1981)	CQ, Mef and QN	-
Dd2	Asia	(Oduola *et al.*, 1988)	-	CQ, Mef and QN
KI	Thailand	(Thaithong & Beale, 1981)	Mef and QN	CQ

Table 1 - Characteristics of clones of *P. falciparum*: 3D7, Dd2, HB3 and K1.
Legend: CQ – chloroquine, Mef – mefloquine, QN – quinine, S - sensitive, R – resistant, ? - There is no identified geographical origin for this clone. [22]

3.2. Microscope

An inverted IX51 microscope from Olympus was used with an oil immersion objective of 100x magnification with a numerical aperture 1.3 and working distance of 0.2 mm. The immersion oil used had a refraction index of 1.3. A drop was placed on the slide and the lens was lifted until it touched the droplet. The oil acted hence as a bridge between the glass plate and the glass lens focusing light rays and preventing dispersion (see figure 4). The larger cone of light entering the lens contributes to increasing the resolution and definition of the image.
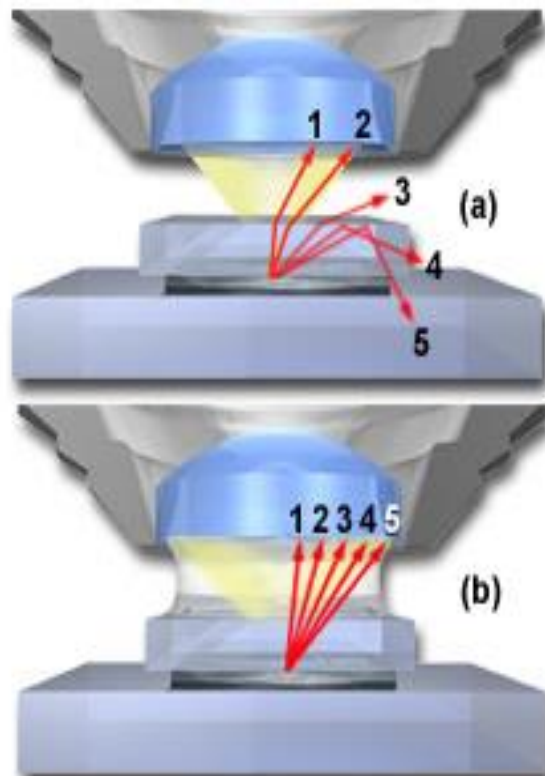
Figure 4 – Passage of light with dry lens (a) and with the use of immersion oil (b) [23].

The quality of an image depends on the resolution and ability of the lens to enlarge the specimen. The resolving power is the ability of the microscope to distinguish between two adjacent points as given by Rayleigh criterion (see equation 1).

$$\rho = \frac{1.22\,\lambda}{NA_{obj} + NA_{cond}} \qquad \text{(Equation 1)}$$

Where ρ is the resolved distance limit, λ is the wavelength of light, NA is the numerical aperture given by $n \times \sin \mu$ - where n is the refractive index of the medium between the object and the lens and where μ is the half-opening angle formed by the optical axis and the external rays of the beam of light penetrating the lens, *obj* is the objective and *cond* is the condenser.

The maximum resolution limit of the optical system employed is approximately 300 nm (for a condenser numerical aperture of 0.95 and considering an average wavelength of 550 nm). As the hemozoin crystals are typically 800x200x200 nm [29], the system cannot resolve the crystals width but can resolve their length. Higher resolution techniques, such as scanning or transmission electron microscopy (SEM and TEM, respectively) require vacuum and are not compatible with living parasites. Figures 5 and 6 show the size and morphology of post-mortem hemozoin crystals.
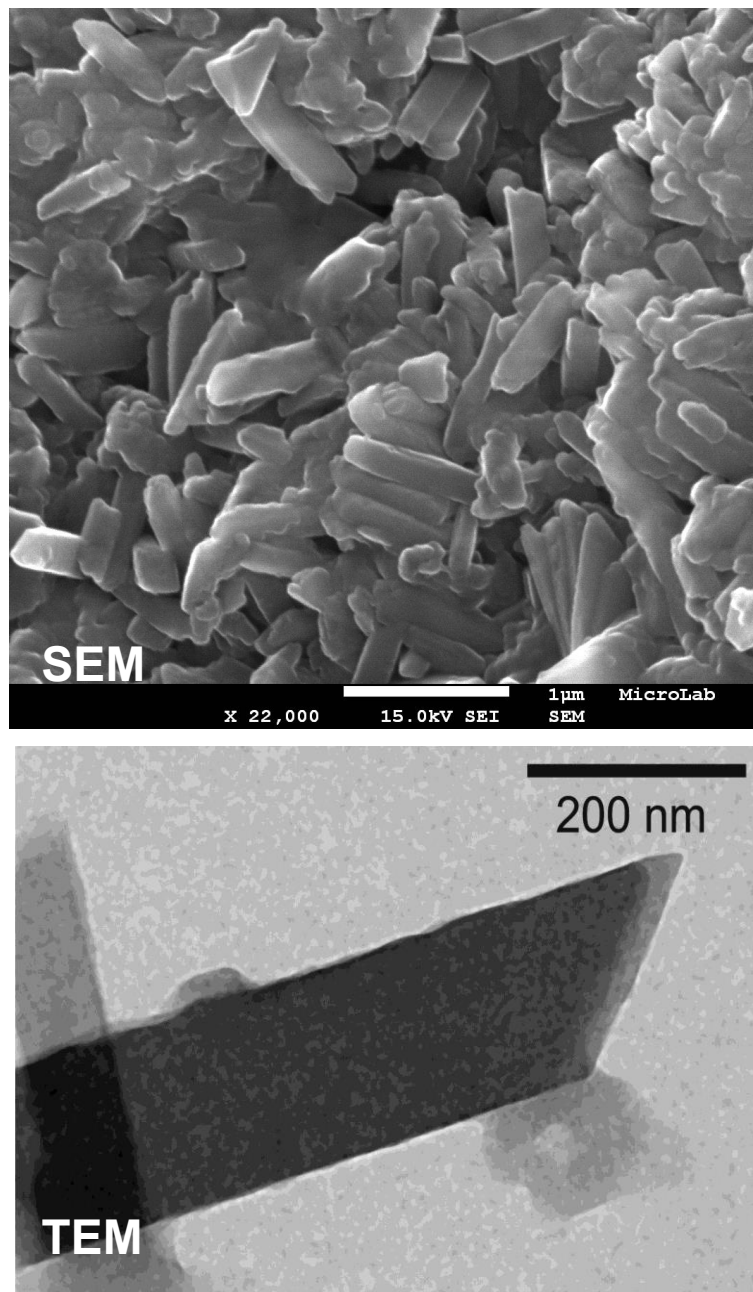
Figure 5 - Scanning (top) and transmission (bottom) electron microscopy images of hemozoin crystals [29].
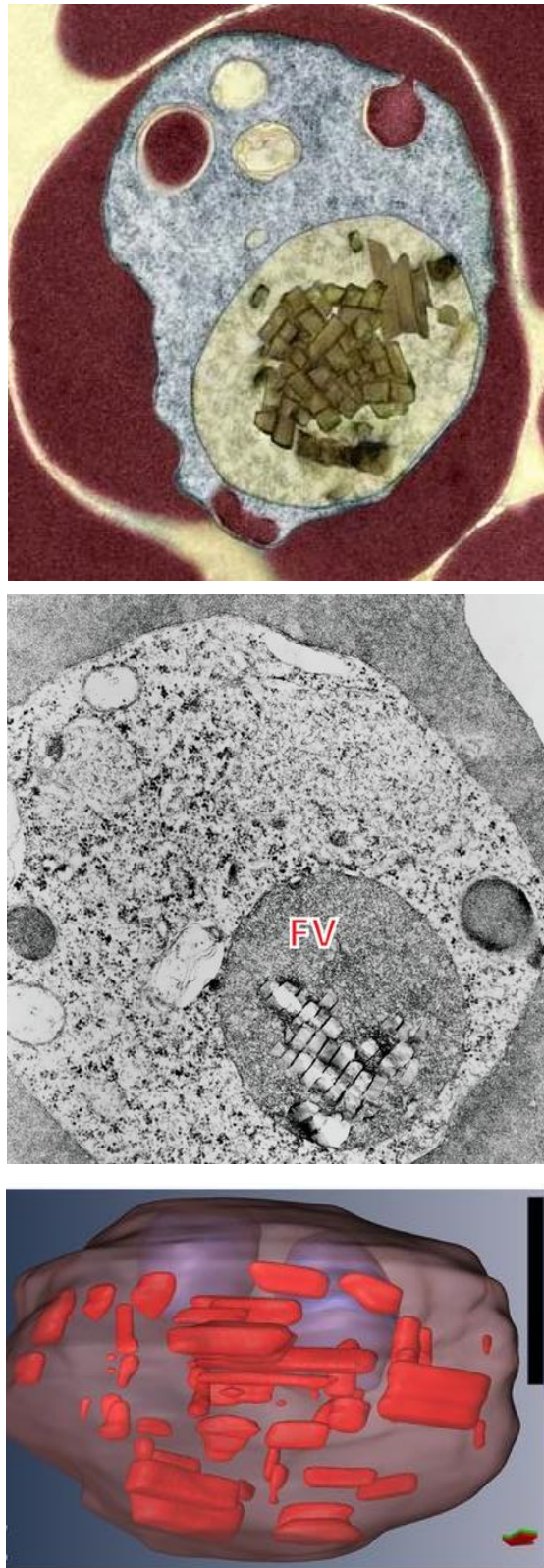
Figure 6 – Hemozoin crystals in the digestive vacuole of post-mortem parasites. (a) Optical microscopy. (b) TEM and (c) TEM tomography. Scale bar: 1 μm. [30-32]. **Legend:** FV – Food Vacuole

The Rayleigh criterion refers to a x,y plane perpendicular to the optical axis, while the resolution at along this axis (z), designated by depth of field (see figure 6), is given by [24]:

$$d = \frac{\lambda \sqrt{n^2 - (NA)^2}}{(NA)^2} \qquad \text{(Equation 2)}$$

Where λ is the wavelength of light, n is the refractive index of the medium between the object and the lens and NA is the numerical aperture of the objective.

Depth of Field Ranges
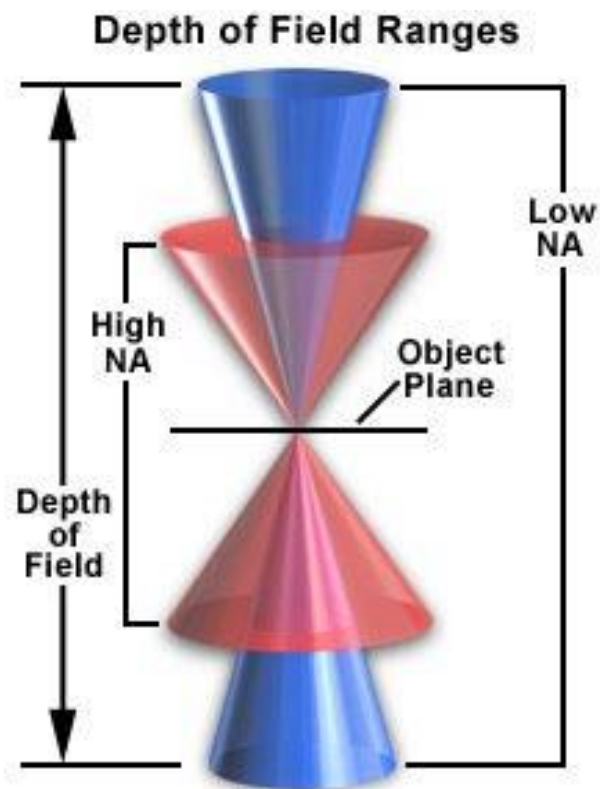
Figure 7 – Depth of field intervals [24].
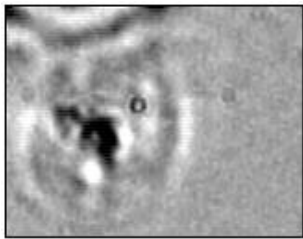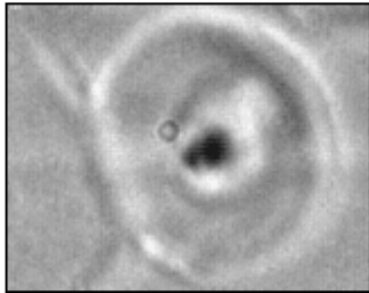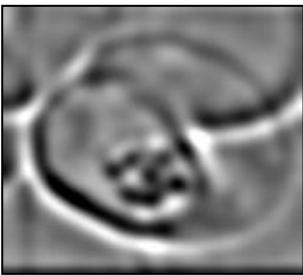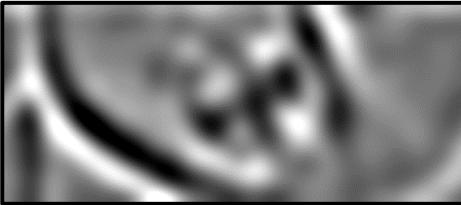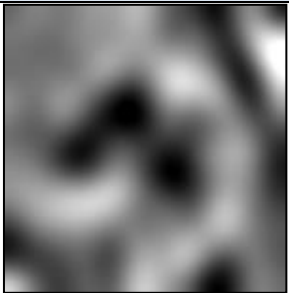
The depth of field of the present system is 253 nm. As the hemozoin crystals are in constant motion their (projected) x,y path can only be tracked within the depth of field.

3.3. Camera

Two high-speed cameras were used in the present work:

- Mega Speed MS70K camera from Canadian Photonics Laboratories with a maximum resolution of 512x512 capable of recording 1 fps to 100,000 fps; [19]
- FastCam SA3 model 120k from Photron with a 1024x1024 pixel resolution at frame rates up to 2,000 fps and at reduced resolution up to 120,000 fps. [20]

Table 2 shows images acquired with the two cameras at different frame rates. As can be seen in table 2, the images acquired with the Mega Speed MS70K camera resulted in lower spatial resolution and, for this reason most of the experiments were carried out using the FastCam camera.

Camera	Frame rate		
Mega Speed MS70K	**2128 fps** (20ºC after culture at 37ºC)	**2128 fps** (20ºC after culture at 37ºC followed by 1h at 41ºC)	
	Frame rate		
FastCam	**4000 fps** (20ºC after culture at 37ºC)	**7500 fps** (20ºC after culture at 37ºC)	**15000 fps (20ºC)** (20ºC after culture at 37ºC)

Table 2 – Images acquired from Mega Speed MS70K and FastCam.

4. Setup for image acquisition

The camera was coupled to the microscope setup as shown in figure 8. The sample was prepared by depositing 50 µl of a diluted cell suspension on a slide previously treated with poly-lysine (this substance provides grip and prevents cell drift under observation). A coverslip was then placed on top of the cell suspension and the set was placed on the microscope stage after depositing a drop of immersion oil on the objective lens. The condenser diaphragm was opened to maximize resolution and after selecting a cell with clearly visible hemozoin crystals the images were acquired at 2128 fps using the Mega Speed camera and at 4000, 7500 and 15000 fps with the FastCam camera. Acquisitions at higher frame rates could not be carried out due to the drastic reduction in intensity and field of view. The movement was characterized at 20ºC for cells kept at healthy body temperature (37ºC) up to the experiment and for cells exposed to febrile temperature (40 ºC or 41 ºC for 1h) immediately prior to the experiments. The measurements were obtained from 10 cells: 7 trophozoites of the 3D7 strain and 3 trophozoites of the Dd2 strain.

Figure 8 – Experimental setup.

4.1. Data processing (ImageJ and MATLAB)

Band pass filtering and segmentation of the images, as well as the determination of the (x,y) projected centroid for each particle, were carried out with a routine developed for ImageJ. (annex 1). The frame sequences were analyzed with routines developed for MATLAB to obtain the following sets of data for each cell studied:

A. The movement of each particle was tracked by direct observation of the frame sequences, and the projected displacement of the centroid between frames was used to describe the path of each particle over time.

B. Since the movement of the particles is strongly affected by noise, the average velocity across path sequences with monotonic variation of both x and y was also determined. An illustrative scheme of a monotonic path sequence is shown in figure 8 (a). The distributions of (i) total displacement and (ii) average velocity in each monotonic sequence are presented in the form of histograms.

C. A graph connecting each particle centroid was obtained for each frame (see figure 8 (b)).

D. The maximum displacement for each tracked particle was used to determine a minorant value for the maximum velocity (see figure 8 (c)).

(a)

(b)

(c)
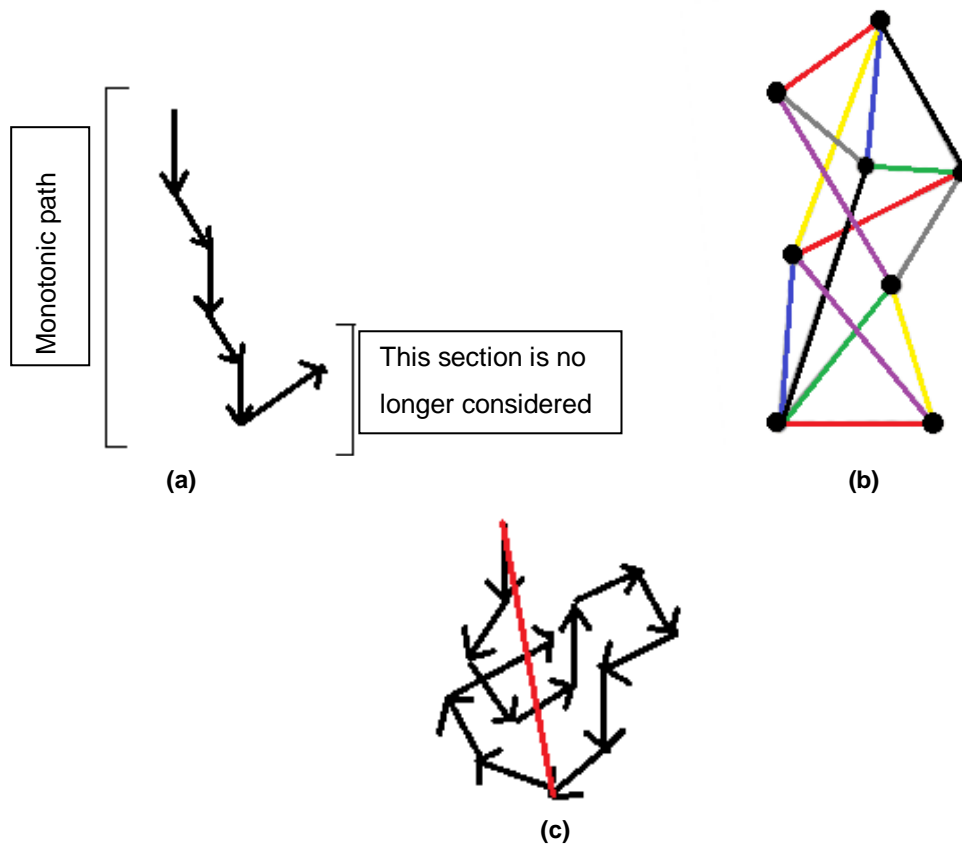
Figure 9 - Illustration of (a) monotonic path, (b) graph connecting all the particle centroids in each frame and (c) maximum displacement.

5.   Results and discussion

5.1. Preliminary experiments with Mega Speed MS70K Camera

Figures 9 and 10 present frames obtained from Cell 1 (3D7 strain) and Cell 2 (3D7 strain), respectively, next to the corresponding segmented image. The trajectory of the tracked particles is compatible with an irregular reciprocating movement and possibly crystal rotation. The image pixelation shows that the spatial resolution of the camera was lower than desirable. The intermittent movement of the particles suggested also that the maximum frame rate for the experimental conditions may be insufficient. For these reasons, the major body of results was obtained with the FastCam camera.
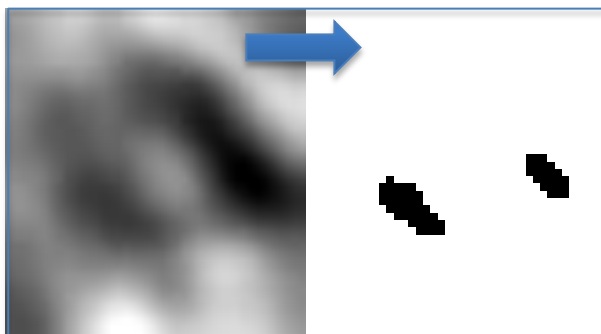
Figure 10 - Cell 1 (3D7 strain) – Sequence of 699 frames (@2128 fps).
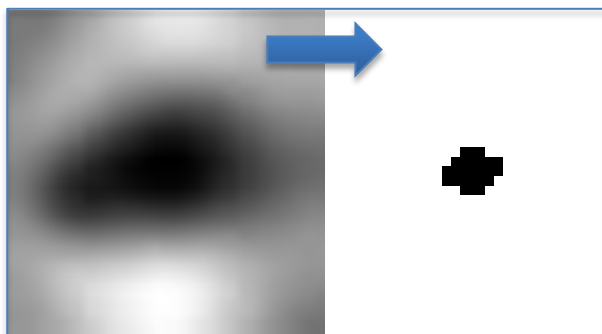
Figure 11 – Cell 2 (3D7 strain) – Sequence of 1001 frames (@2128 fps).

5.2. FastCam Camera

Figures 11 to 18 present frames of sequences obtained at different frame rates from Cell 3 to Cell 10 next to the corresponding segmented image. The centroid of each spot were subsequently determined for each frame. These results showed enhanced spatial and temporal resolutions when compared with the previous ones. Although the dark spots in the frames may not always correspond to individual particles (compare figures 6 and 12 to 19), for simplicity the words particle and spot will be used interchangeably in the following analysis. Nonetheless, the nature of the images (dark isolated spots in a bright background) enabled to track the movement with a resolution higher to what is established by the Rayleigh criterion defined for two contiguous points with similar contrast.
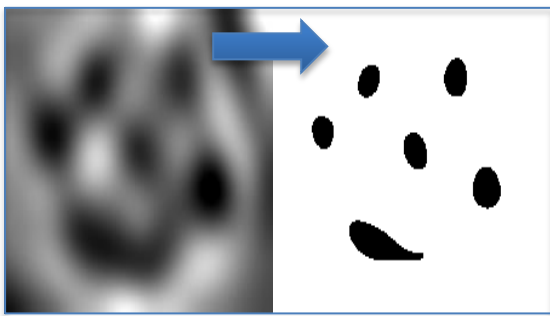
Figure 12 - Cell 3 (3D7 strain) – Sequence of 409 frames (@4000 fps)
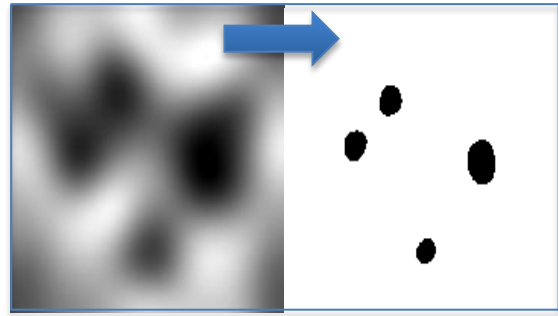
Figure 13 - Cell 4 (3D7 strain) – Sequence of 394 frames (@4000 fps)
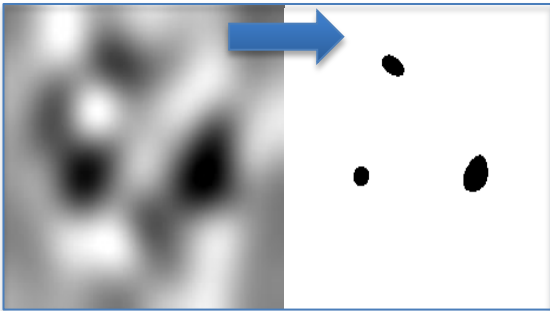
Figure 14 - Cell 5 (3D7 strain) – Sequence of 423 frames (@4000 fps)
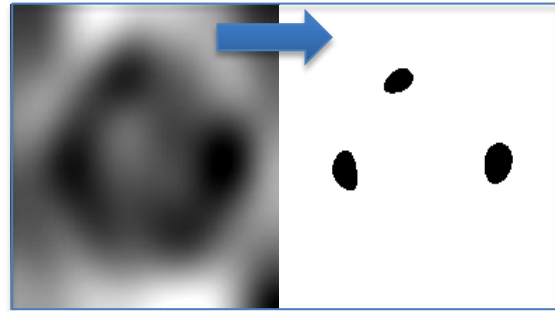
Figure 15 - Cell 6 (3D7 strain) – Sequence of 310 frames (@4000 fps)
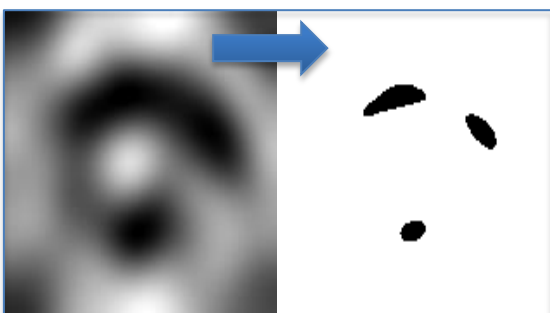
Figure 16 - Cell 7 (3D7 strain) – Sequence of 338 frames (@4000 fps)
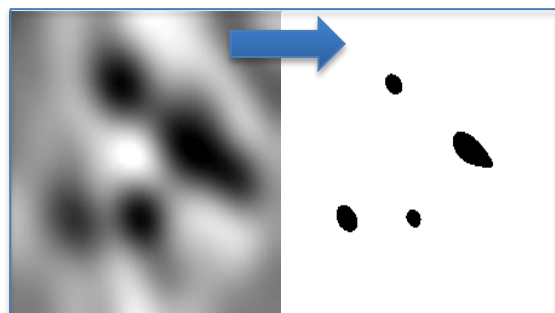
Figure 17 - Cell 8 (Dd2 strain) – Sequence of 226 frames (@4000 fps)
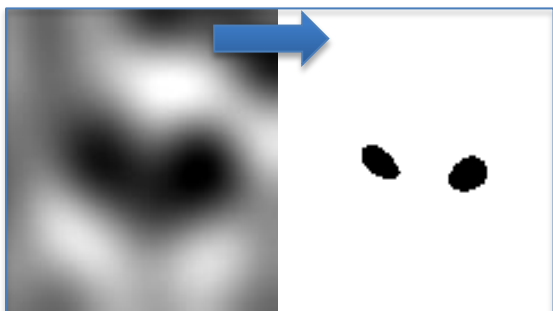
Figure 18 - Cell 9 (Dd2 strain) – Sequence of 226 frames (@4000 fps)
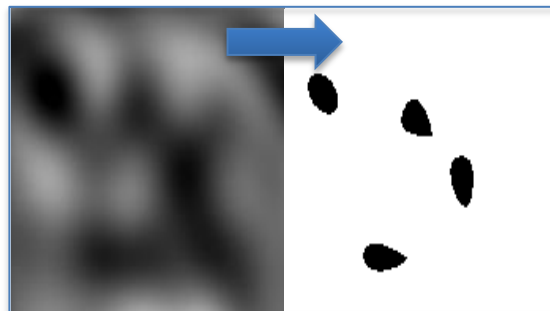
Figure 19 - Cell 10 (Dd2 strain) – Sequence of 282 frames (@4000 fps)

Figures 20 to 61 present the following results for each of the cells investigated:

A. Projected displacement of particle centroids tracked along the sequences acquired at a given frame rate. The pixel size was 10 nm and 12 nm for, respectively, the 3D7 and Dd2 strains. The displacements of each centroid are projected with a different color in a common graph for each cell and displacement distributions (in pixels) are presented in the form of histograms.

B. Histograms of total displacement and average velocity in each monotonic sequence. The bin size used was proportional to the frame rate to normalize the effect of this variable.

C. Overlapped graphs connecting all centroids in each frame (colors have been added for clarity and have no physical meaning).

5.2.1. Cell 3
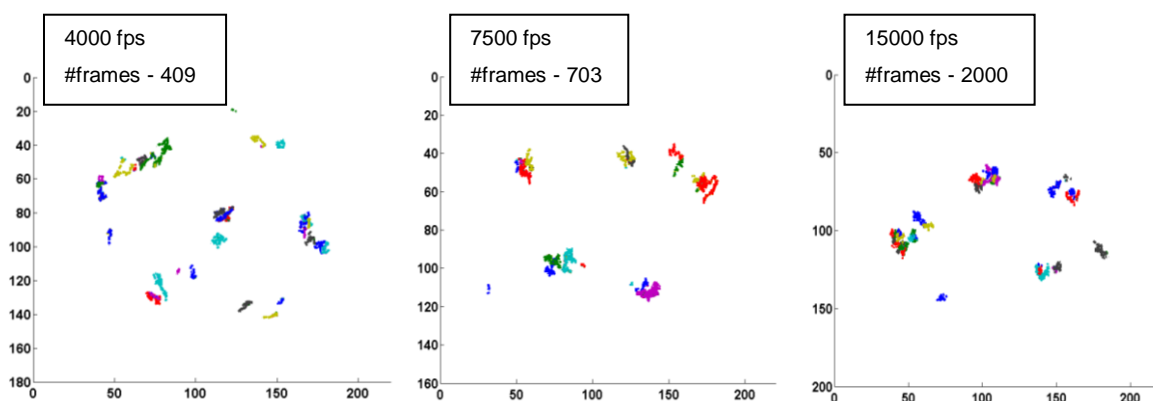
Figure 20 – <u>Cell 3 (3D7 strain)</u> - Displacement (projected) of each centroid over time. Each color represents the path of an individual particle during a given frame sequence.
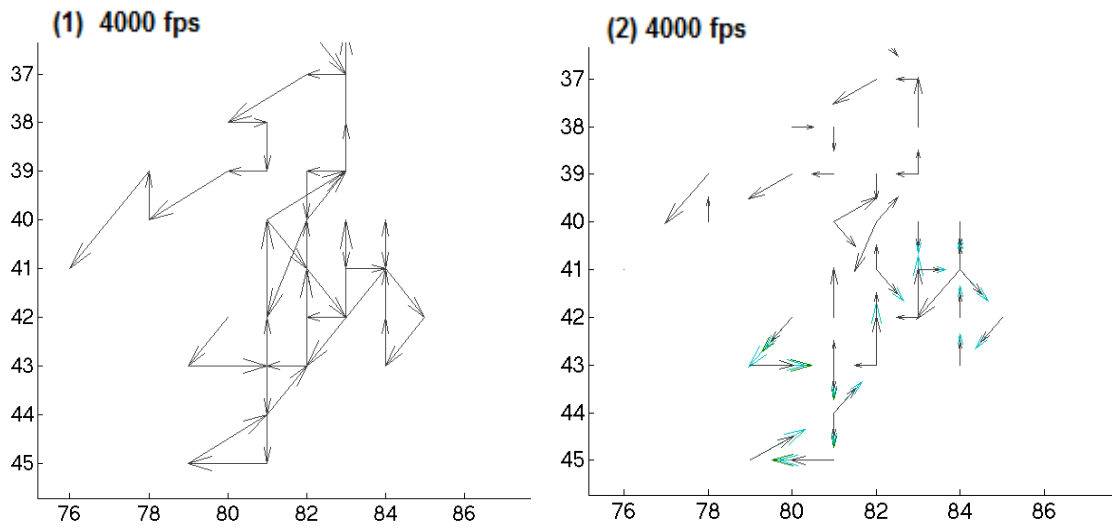
Figure 21 – <u>Cell 3 (3D7 strain)</u> – Magnification showing in detail the path of a tracked particle: (1) Scaled vectors and (2) "Rescaled" vectors to expose overlapping.
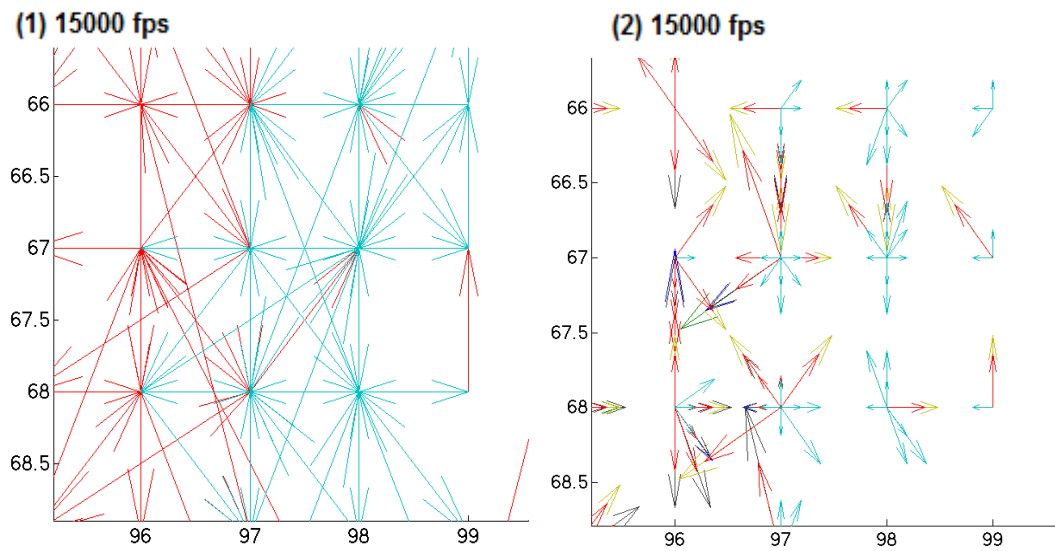
Figure 22 – (1) <u>Cell 3 (3D7 strain)</u> - Magnification showing in detail the path of a tracked particle Scaled vectors and (2) "Rescaled" vectors to expose overlapping.

Figure 23 – <u>Cell 3 (3D7 strain)</u> - Projected displacement of centroids between frames.

Figure 24 – <u>Cell 3 (3D7 strain)</u> - Distribution of average displacement across monotonic paths.

Figure 25 – <u>Cell 3 (3D7 strain)</u> - Distribution of the average velocity across monotonic paths. The bin size used is proportional to the frame rate to normalize the effect of this variable.

Figure 26 - <u>Cell 3 (3D7 strain)</u> - Overlapping graphs of each frame.

5.2.2. Cell 4

Figure 27 – <u>Cell 4 (3D7 strain)</u> - Displacement (projected) of each centroid over time. Each color represents the path of an individual particle during a given frame sequence.

Figure 28 – <u>Cell 4 (3D7 strain)</u> - Projected displacement of centroids between frames.

Figure 29 – <u>Cell 4 (3D7 strain)</u> - Distribution of average displacement across monotonic paths.

Figure 30 – <u>Cell 4 (3D7 strain)</u> - Distribution of the average velocity across monotonic paths. The bin size used is proportional to the frame rate to normalize the effect of this variable.

Figure 31 – <u>Cell 4 (3D7 strain)</u> - Overlapping graphs of each frame.

5.2.3. Cell 5

Figure 32 – <u>Cell 5 (3D7 strain)</u> - Displacement (projected) of each centroid over time. Each color represents the path of an individual particle during a given frame sequence.

Figure 33 – <u>Cell 5 (3D7 strain)</u> - Projected displacement of centroids between frames.

Figure 34 – <u>Cell 5 (3D7 strain)</u> - Distribution of average displacement across monotonic paths.

Figure boxes text:

4000 fps
f_m = 33/74
#anf – 3.3
#frames – 423
$\overline{v} = 38.7 + 11.6\,\mathrm{um/s}$

7500 fps
f_m = 43/103
#anf – 3.3
#frames – 682
$\overline{v} = 70.6 + 24.1\,\mathrm{um/s}$

15000 fps
f_m = 187/432
#anf – 3.2
#frames – 2000
$\overline{v} = 150.9 + 56.1\,\mathrm{um/s}$

Figure 35 – <u>Cell 5 (3D7 strain)</u> - Distribution of the average velocity across monotonic paths. The bin size used is proportional to the frame rate to normalize the effect of this variable.

4000 fps
#frames - 423

7500 fps
#frames - 682

15000 fps
#frames - 2000

Figure 36 – <u>Cell 5 (3D7 strain)</u> - Overlapping graphs of each frame.

5.2.4. Cell 6

4000 fps
#frames - 310

7500 fps
#frames - 593

15000 fps
#frames - 2000

Figure 37 – <u>Cell 6 (3D7 strain)</u> - Displacement (projected) of each centroid over time. Each color represents the path of an individual particle during a given frame sequence.
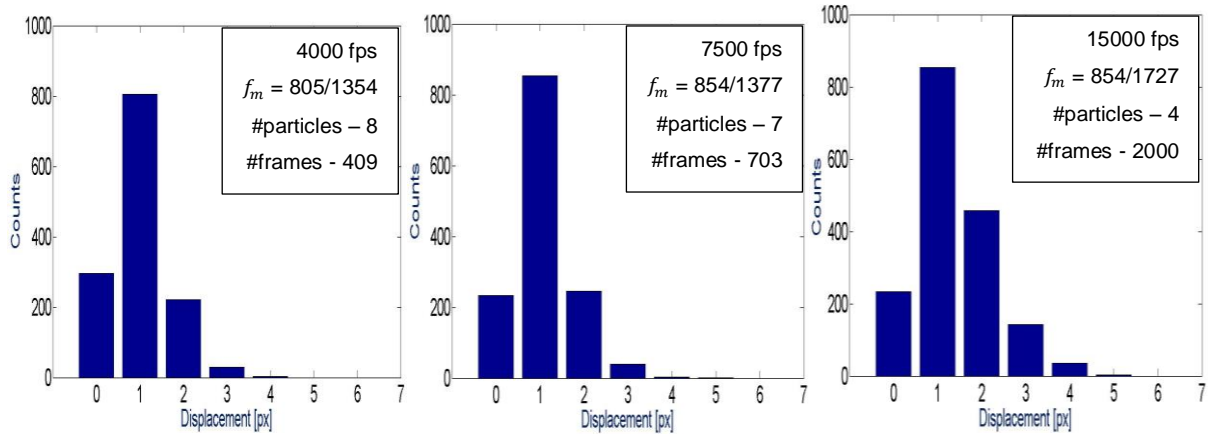
Figure 38 – <u>Cell 6 (3D7 strain)</u> - Projected displacement of centroids between frames.
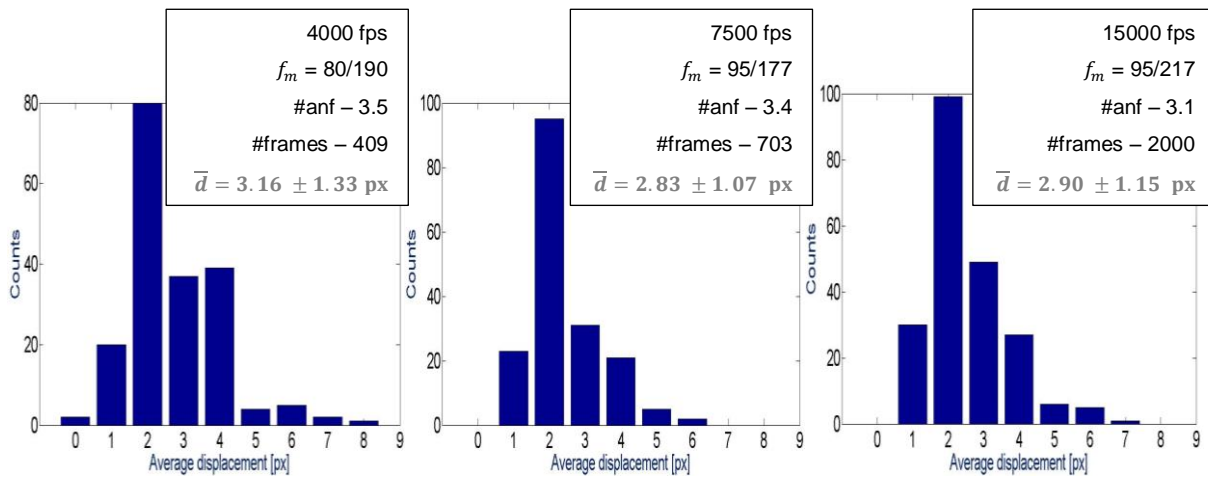

Figure 39 – <u>Cell 6 (3D7 strain)</u> - Distribution of average displacement across monotonic paths.
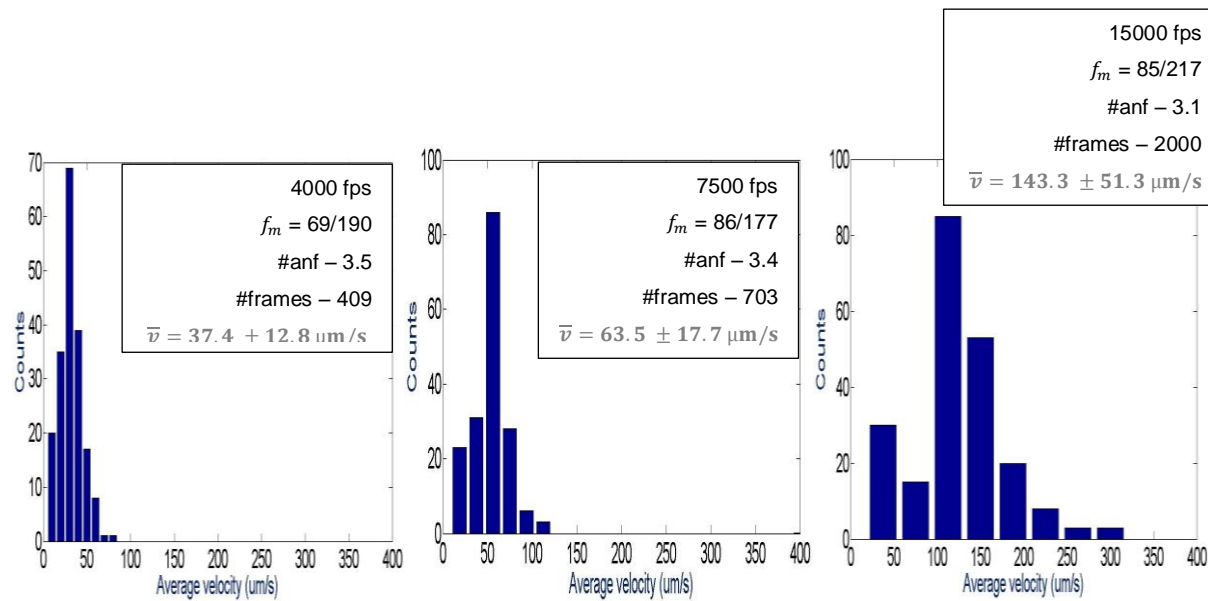

Figure 40 – <u>Cell 6 (3D7 strain)</u> - Distribution of the average velocity across monotonic paths. The bin size used is proportional to the frame rate to normalize the effect of this variable.
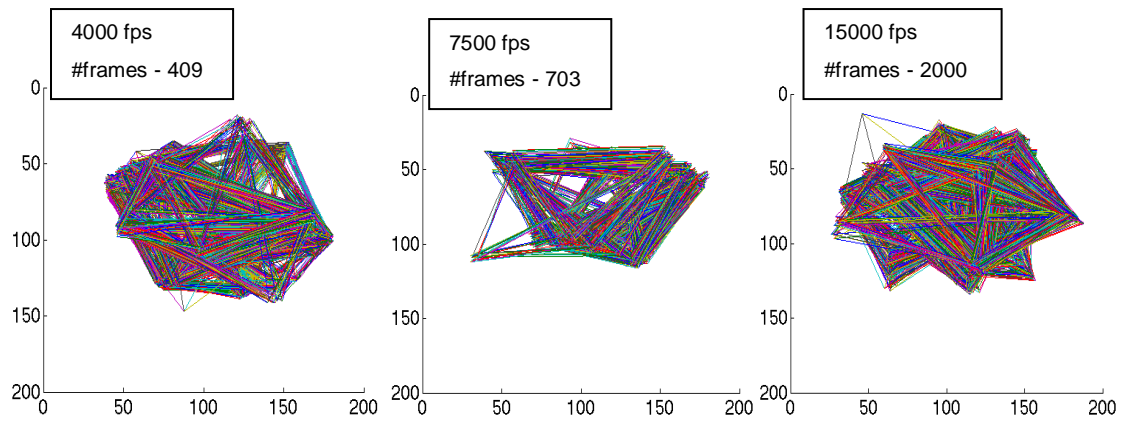
Figure 41 – <u>Cell 6 (3D7 strain)</u> - Overlapping graphs of each frame.
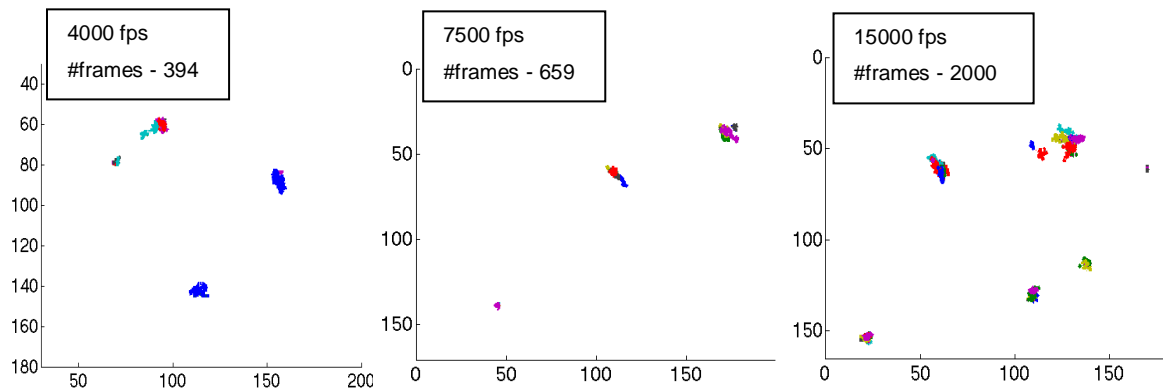
5.2.5. Cell 7

Figure 42 – <u>Cell 7 (3D7 strain)</u> - Displacement (projected) of each centroid over time. Each color represents the path of an individual particle during a given frame sequence.
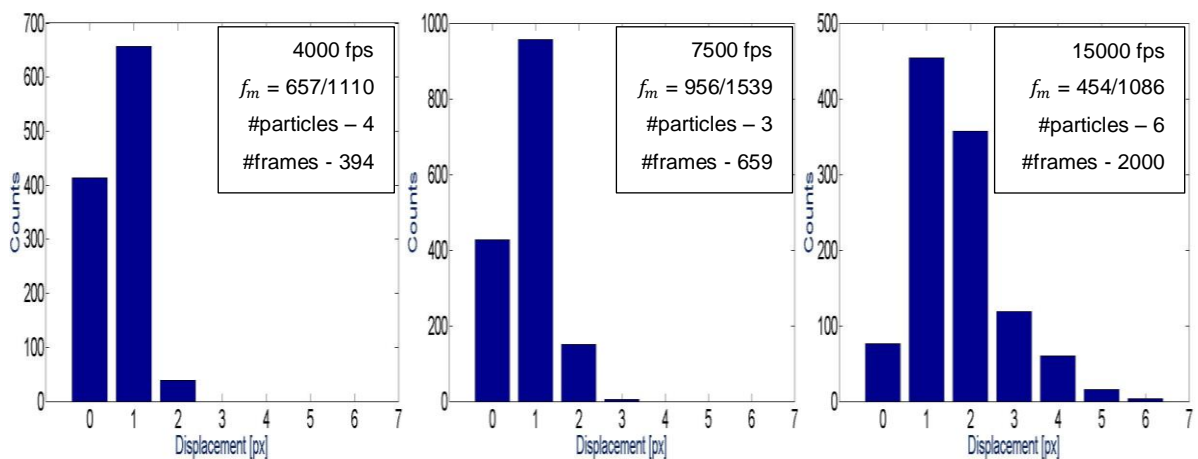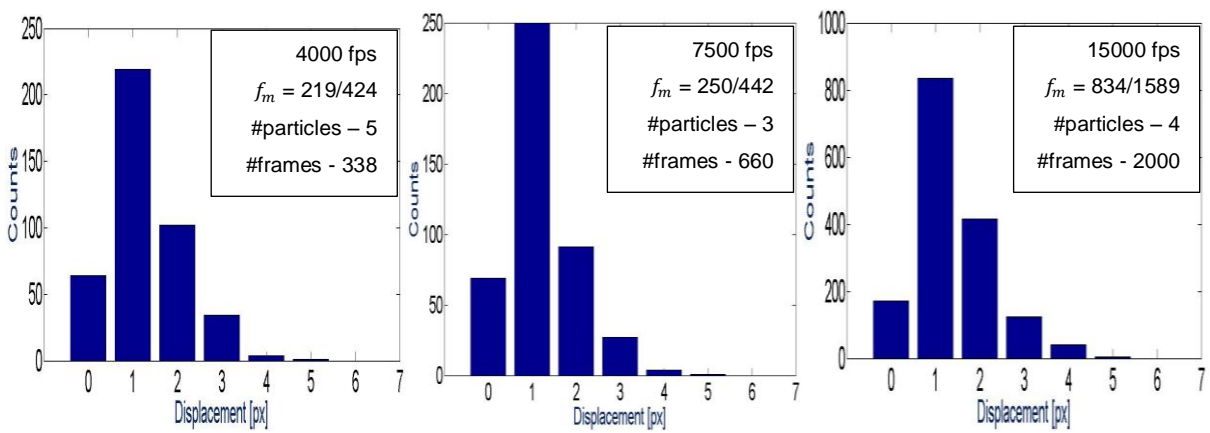

Figure 43 – <u>Cell 7 (3D7 strain)</u> - Projected displacement of centroids between frames.

Figure 44 – <u>Cell 7 (3D7 strain)</u> - Distribution of average displacement across monotonic paths.

Figure 45 – <u>Cell 7 (3D7 strain)</u> - Distribution of the average velocity across monotonic paths. The bin size used is proportional to the frame rate to normalize the effect of this variable.
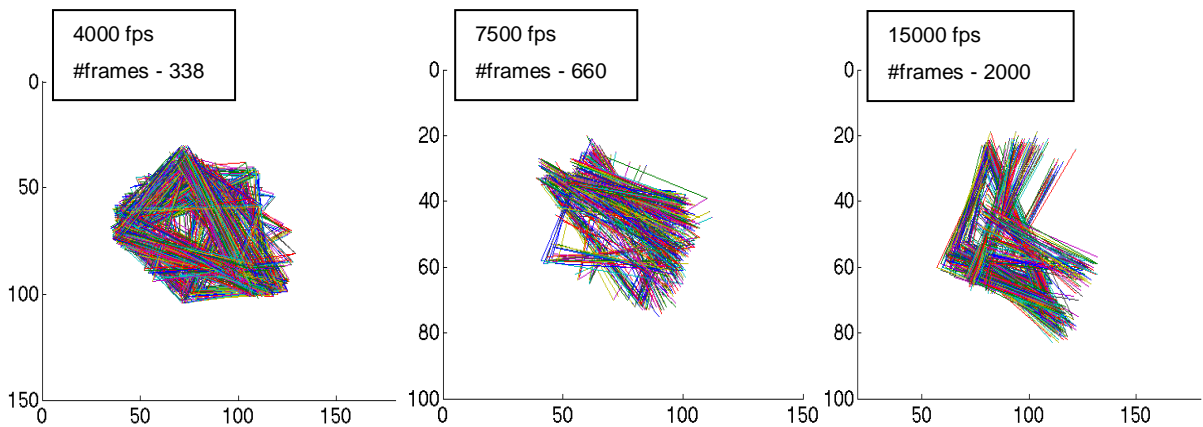
Figure 46 – <u>Cell 7 (3D7 strain)</u> - Overlapping graphs of each frame.

5.2.6. Cell 8
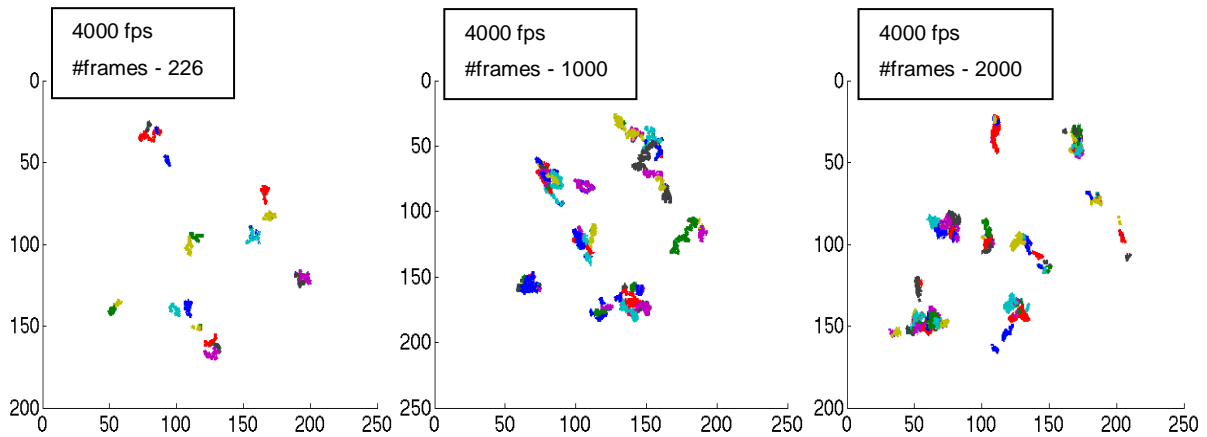
Figure 47 – <u>Cell 8 (Dd2 strain)</u> - Displacement (projected) of each centroid over time. Each color represents the path of an individual particle during a given frame sequence.
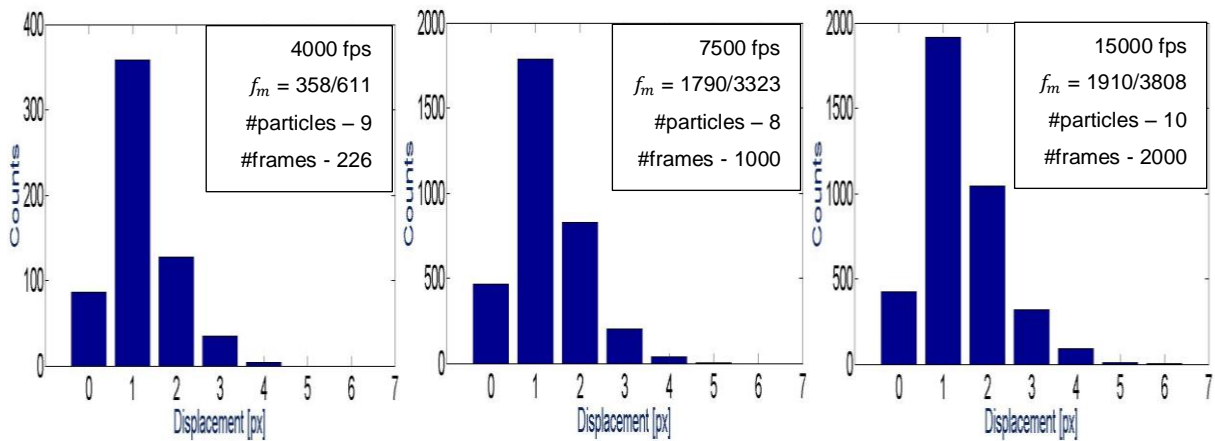
Figure 48 – <u>Cell 8 (Dd2 strain)</u> - Projected displacement of centroids between frames.
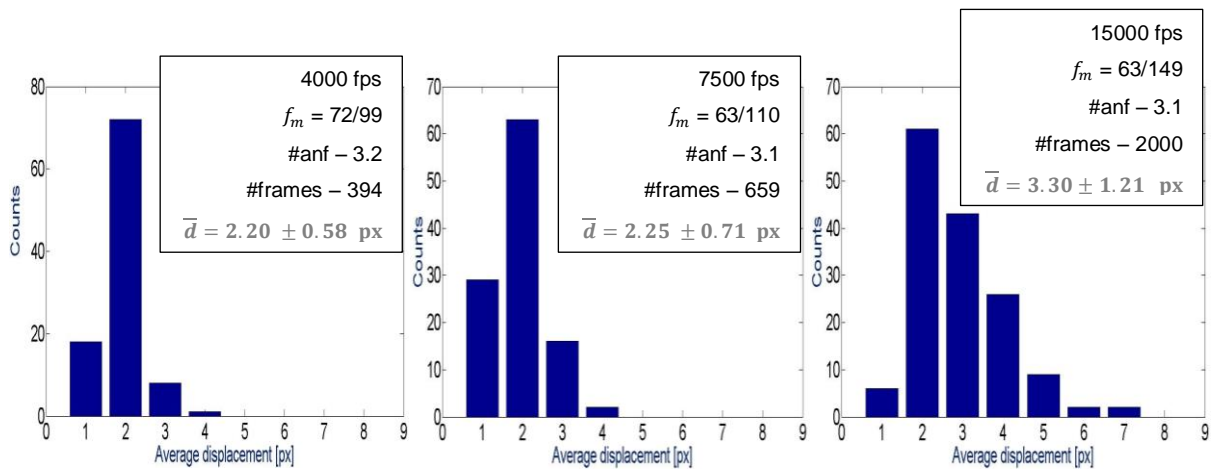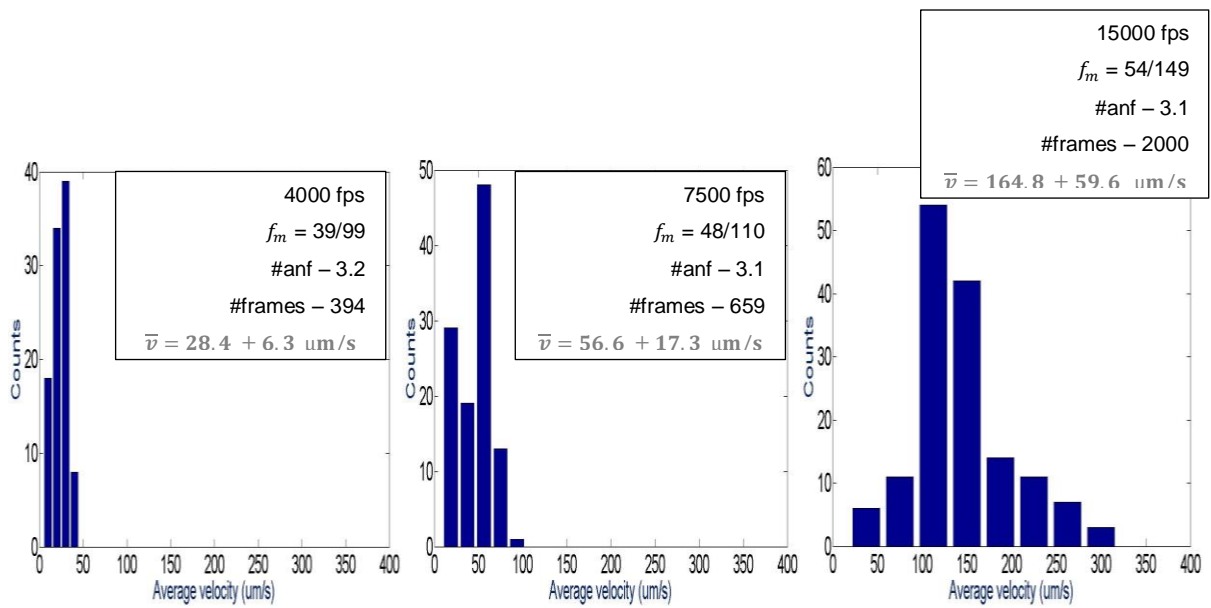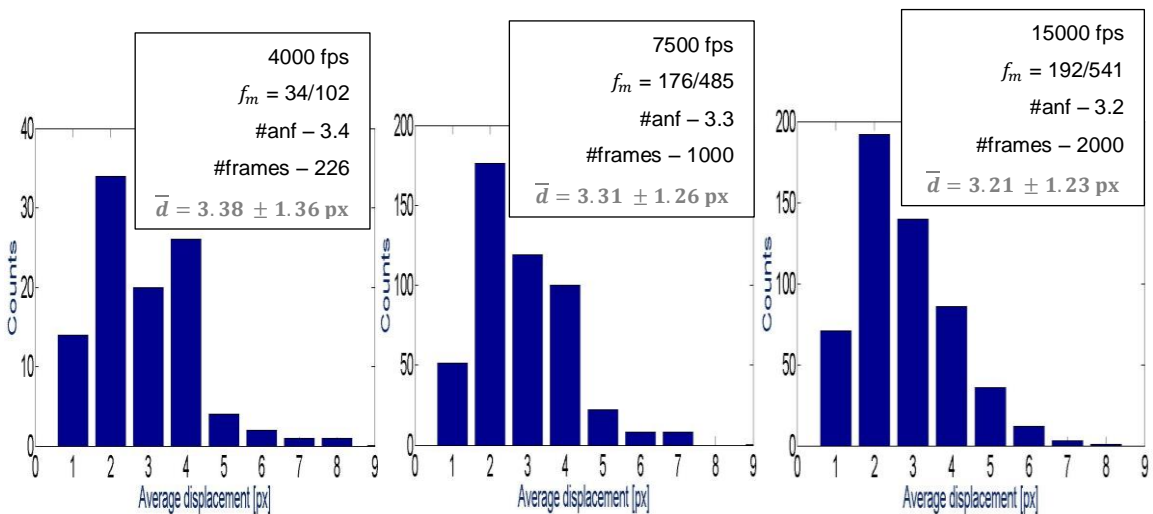

Figure 49 – <u>Cell 8 (Dd2 strain)</u> - Distribution of average displacement across monotonic paths.
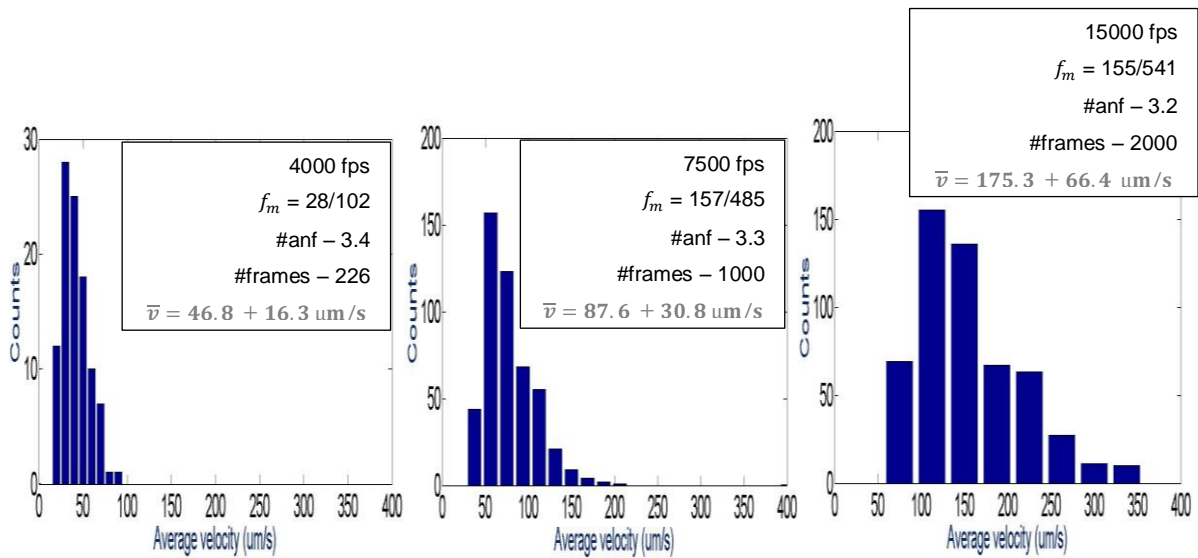
Figure 50 – <u>Cell 8 (Dd2 strain)</u> - Distribution of the average velocity across monotonic paths. The bin size used is proportional to the frame rate to normalize the effect of this variable.
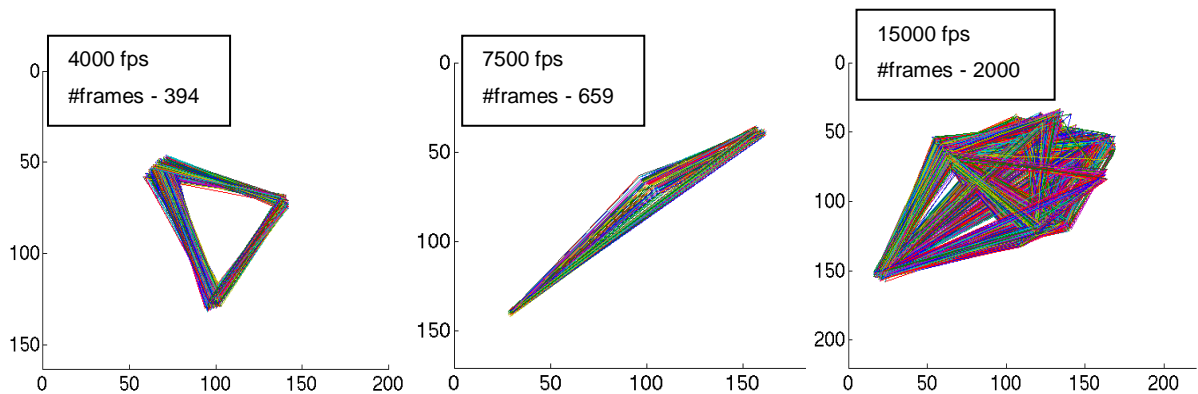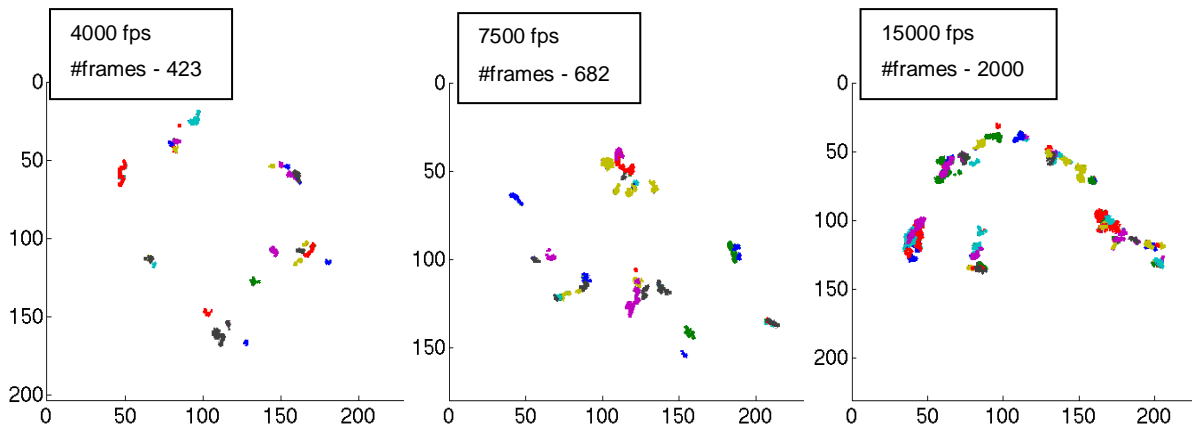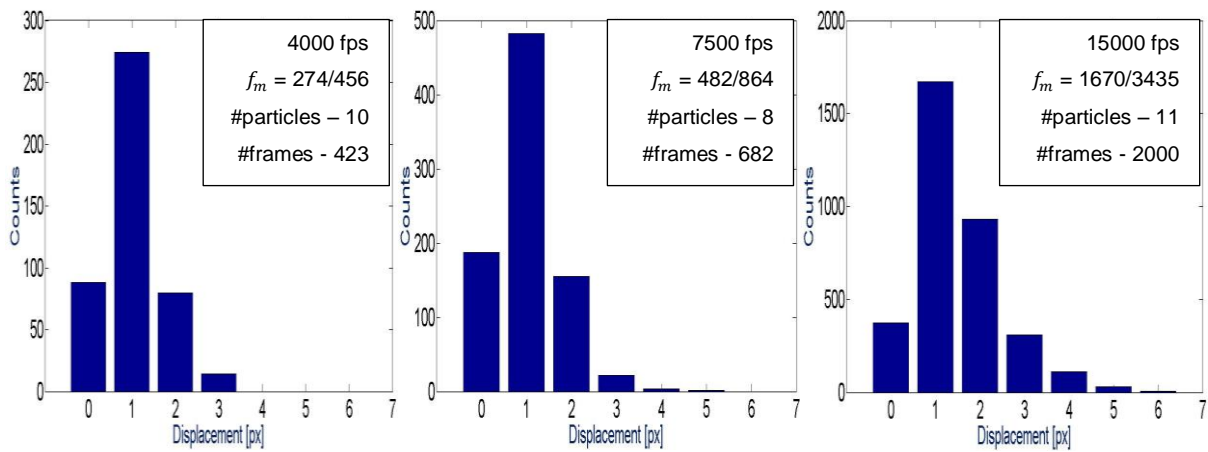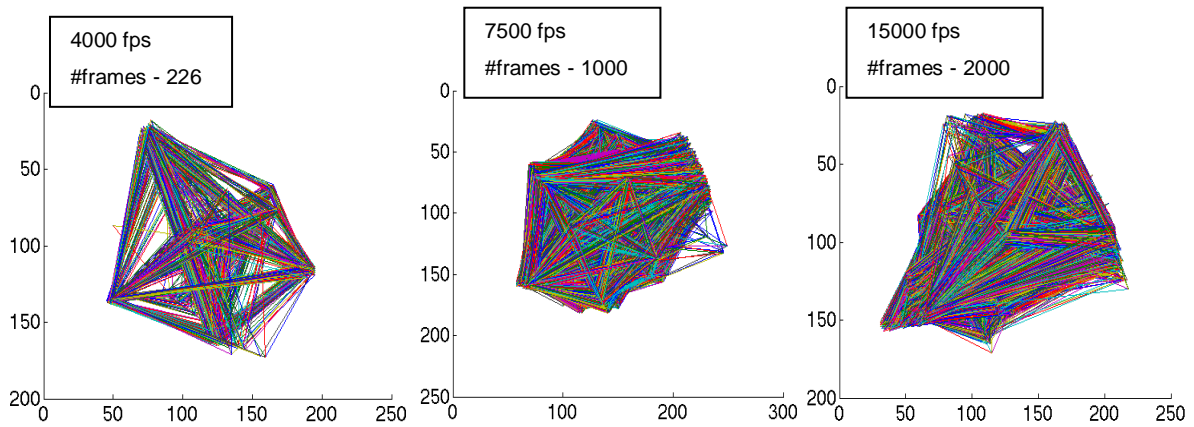

Figure 51 – <u>Cell 8 (Dd2 strain)</u> - Overlapping graphs of each frame.
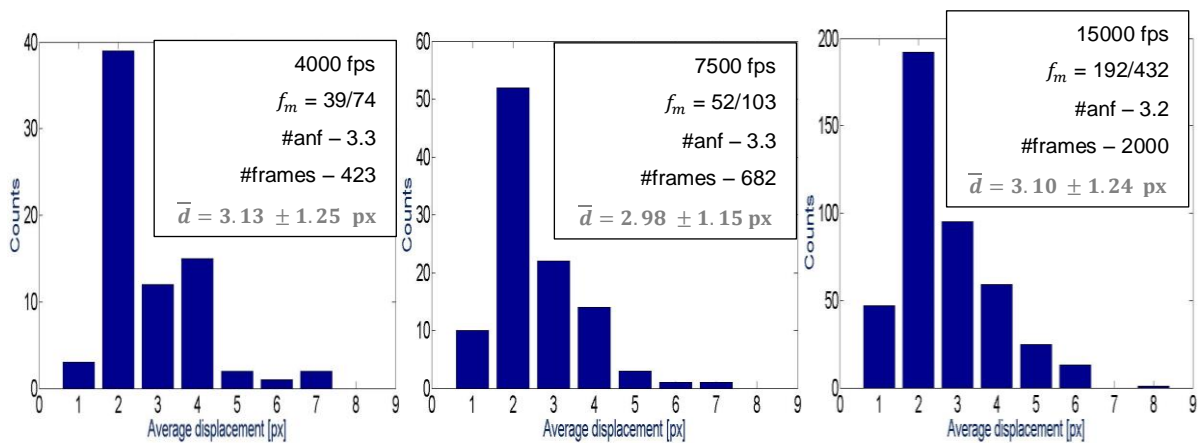
5.2.7. Cell 9
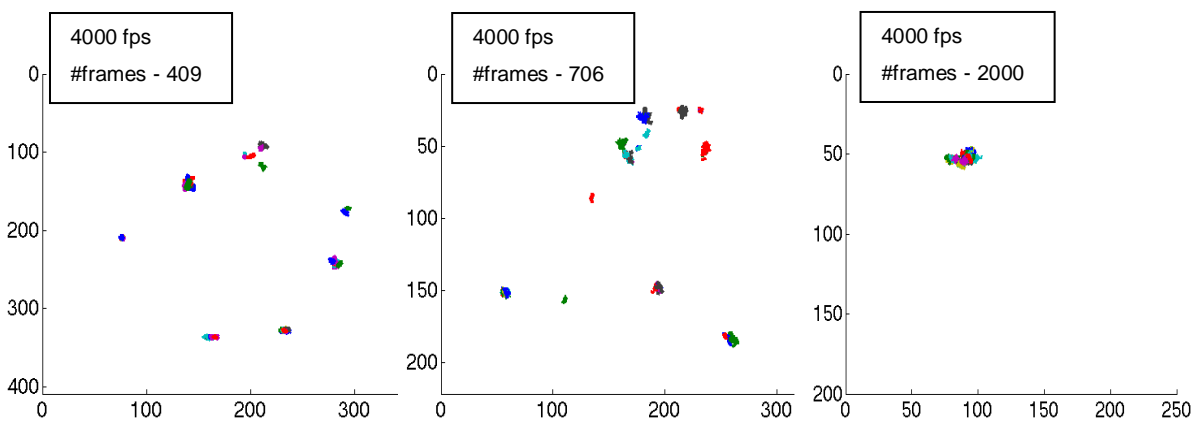
Figure 52 – <u>Cell 9 (Dd2 strain)</u> - Displacement (projected) of each centroid over time. Each color represents the path of an individual particle during a given frame sequence.
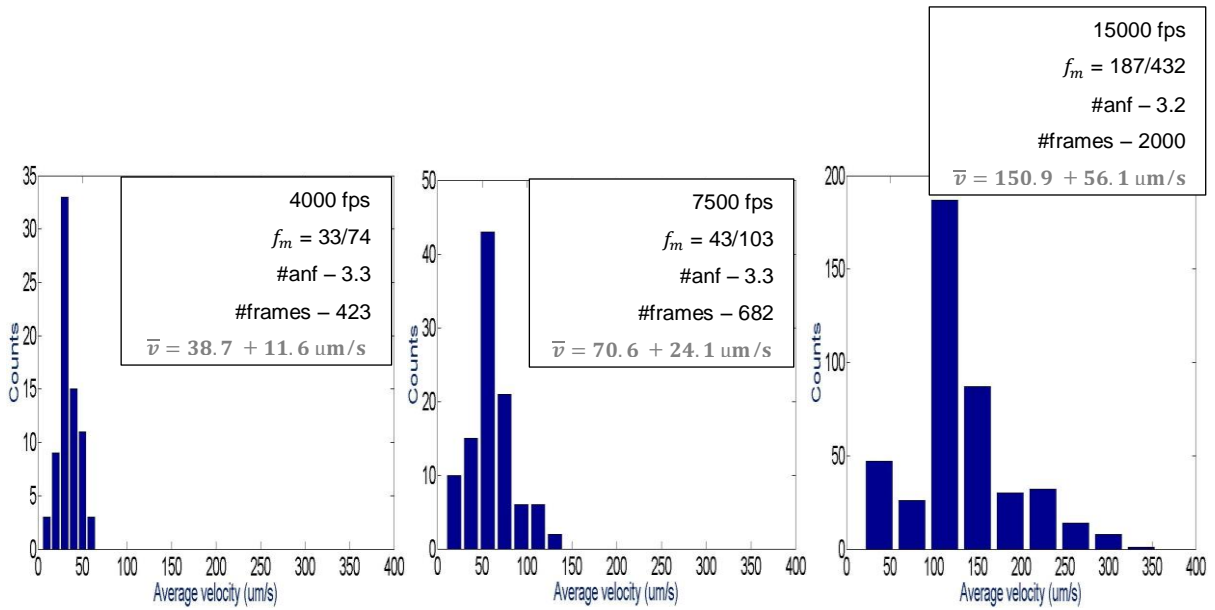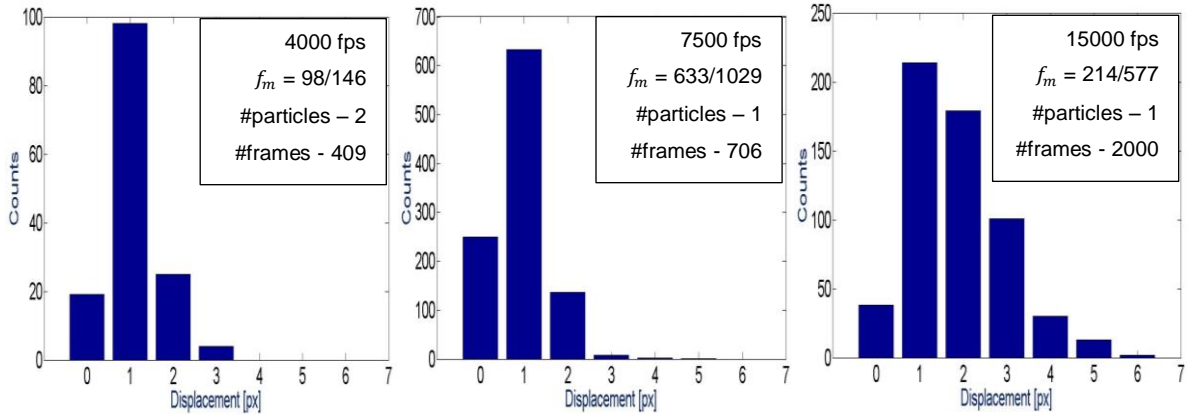
Figure 53 – <u>Cell 9 (Dd2 strain)</u> - Projected displacement of centroids between frames.
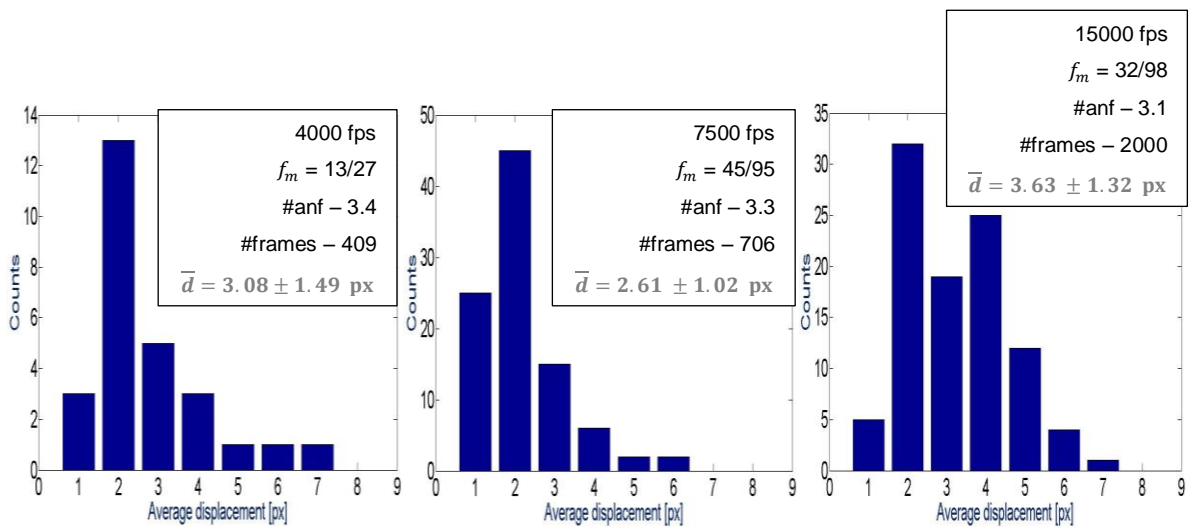
Figure 54 – <u>Cell 9 (Dd2 strain)</u> – Distribution of average displacement across monotonic paths.
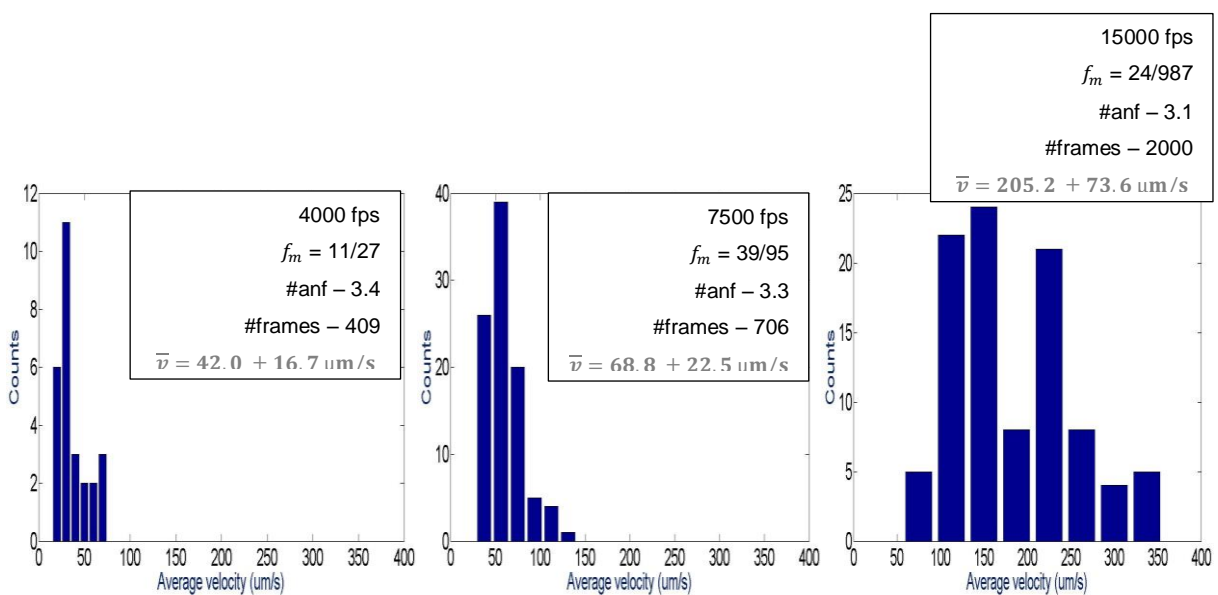
Figure 55 – <u>Cell 9 (Dd2 strain)</u> - Distribution of the average velocity across monotonic paths. The bin size used is proportional to the frame rate to normalize the effect of this variable.
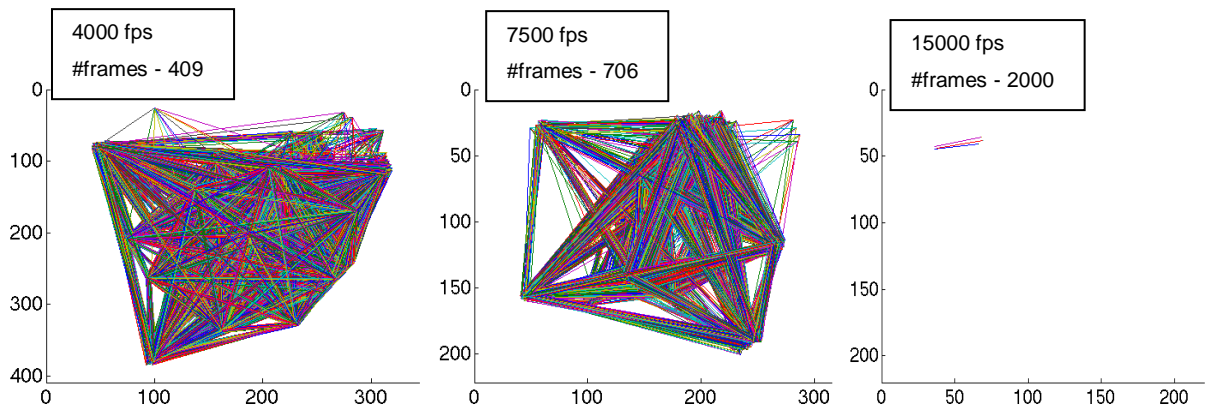
Figure 56 – <u>Cell 9 (Dd2 strain)</u> - Overlapping graphs of each frame.

5.2.8. Cell 10
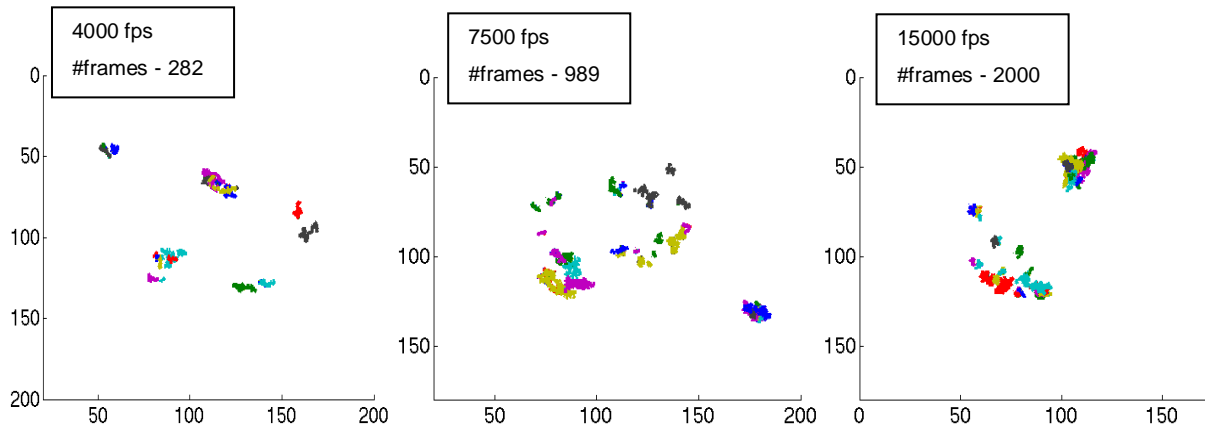
Figure 57 – <u>Cell 10 (Dd2 strain)</u> - Displacement (projected) of each centroid over time. Each color represents the path of an individual particle during a given frame sequence.
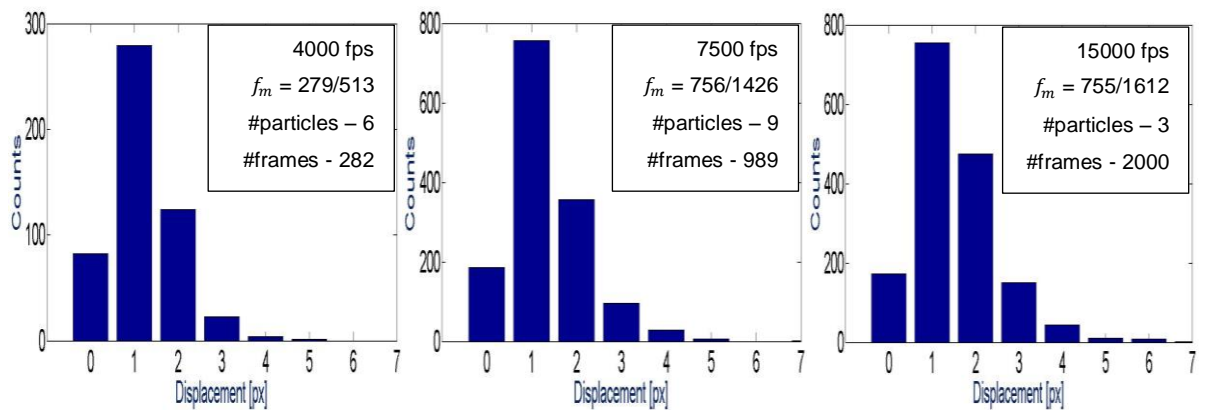
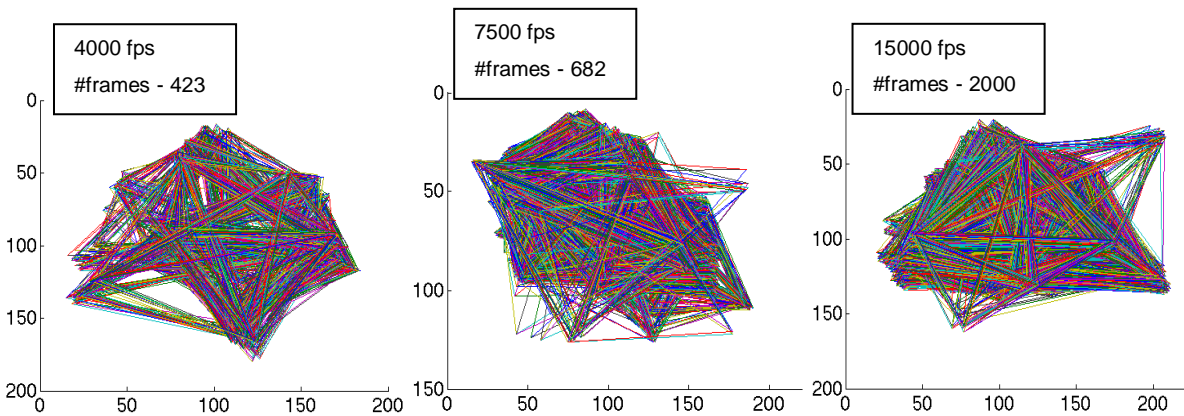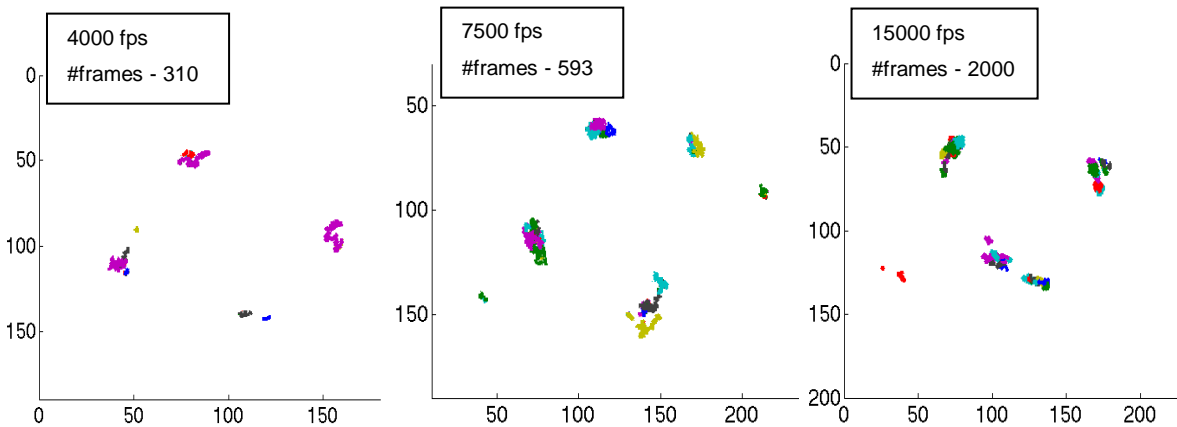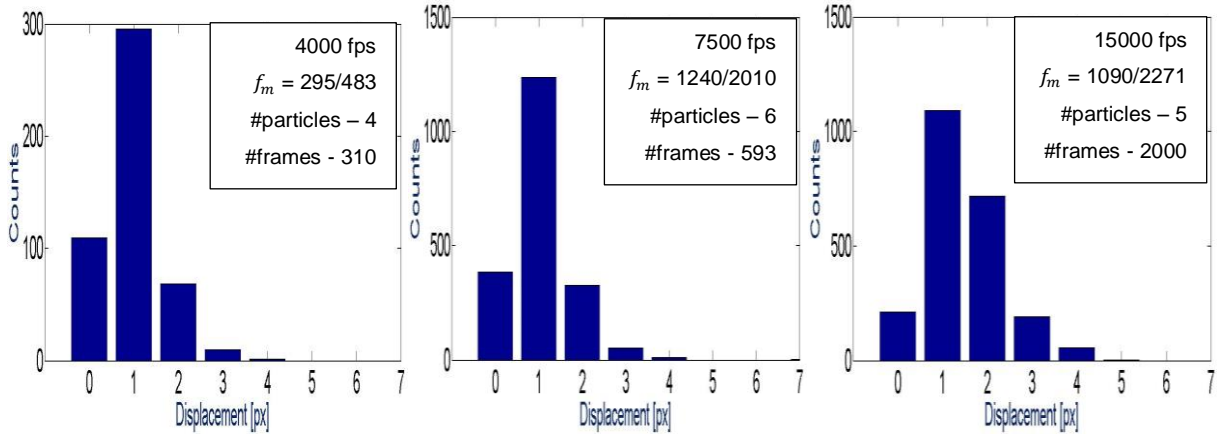**Figure 58** – <u>Cell 10 (Dd2 strain)</u> - Projected displacement of centroids between frames.
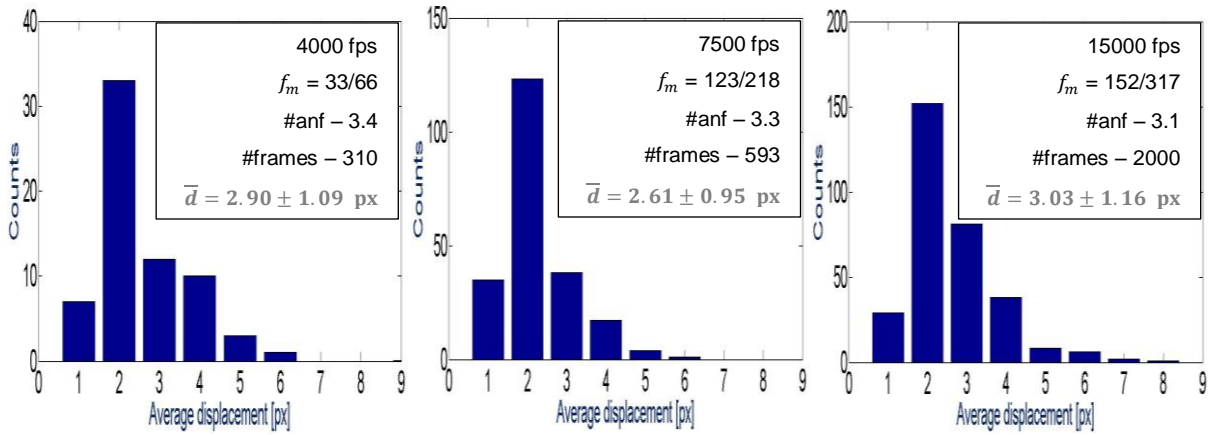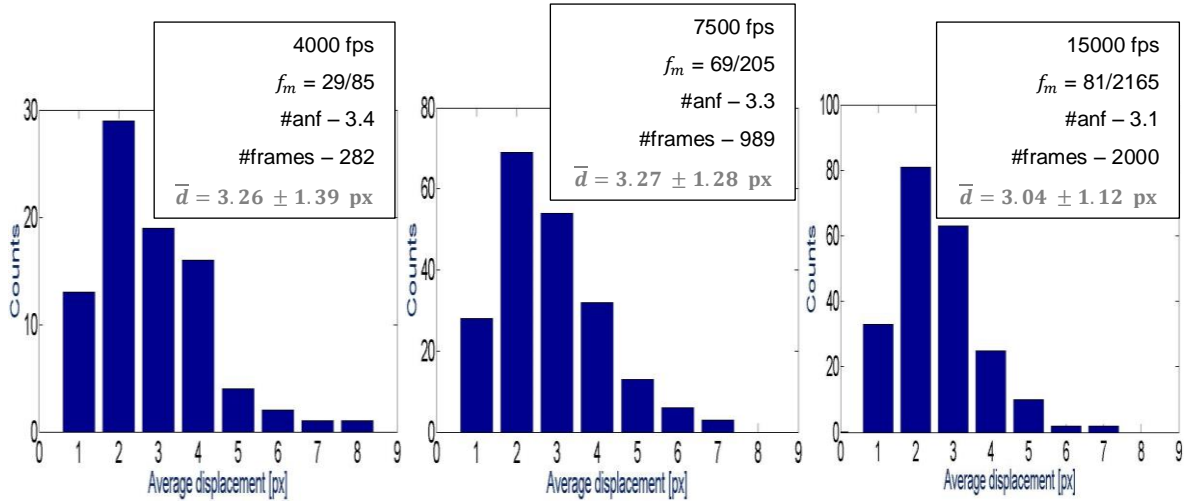
Figure 59 – <u>Cell 10 (Dd2 strain)</u> - Distribution of average displacement across monotonic paths.
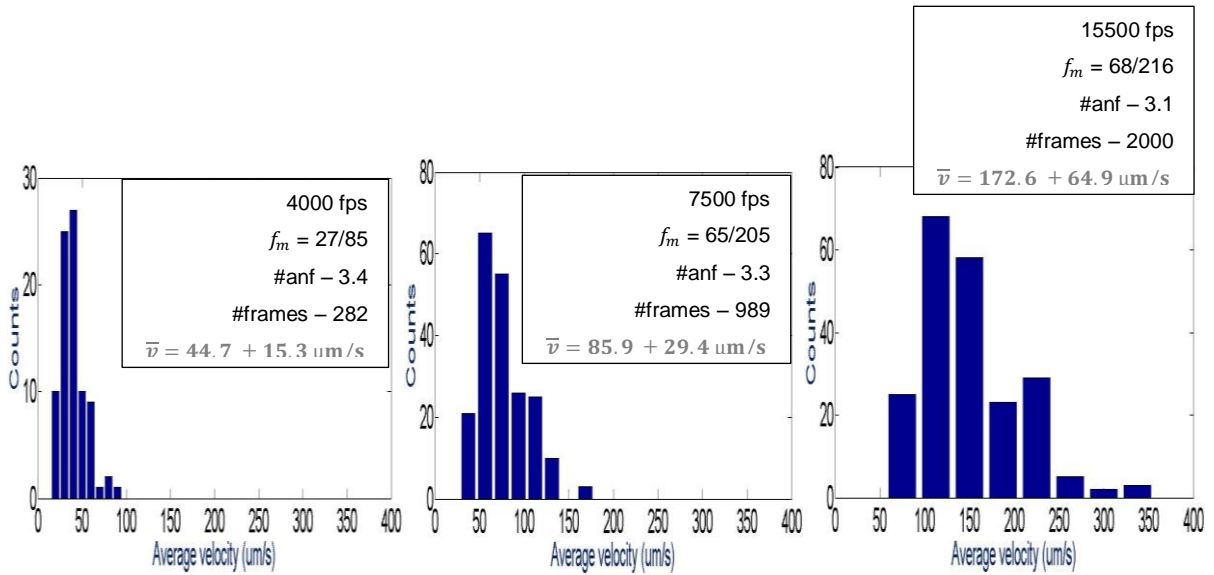
Figure 60 – <u>Cell 10 (Dd2 strain)</u> - Distribution of the average velocity across monotonic paths. The bin size used is proportional to the frame rate to normalize the effect of this variable.
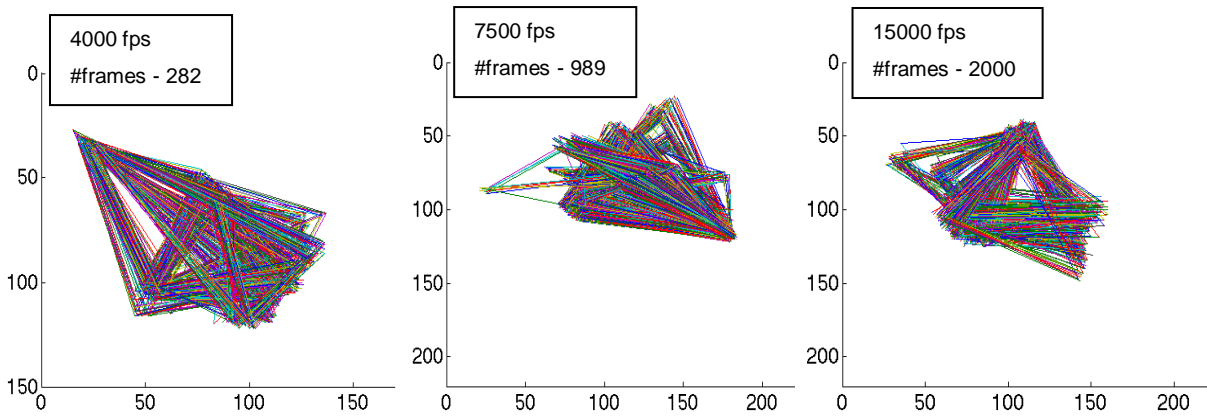
Figure 61 – <u>Cell 10 (Dd2 strain)</u> - Overlapping graphs of each frame.

5.2.9. Global distributions for the 3D7 strain

Figures 62 to 64 present the global results of the analyses for the 3D7 strain and a summary is presented in tables 3 and 4.
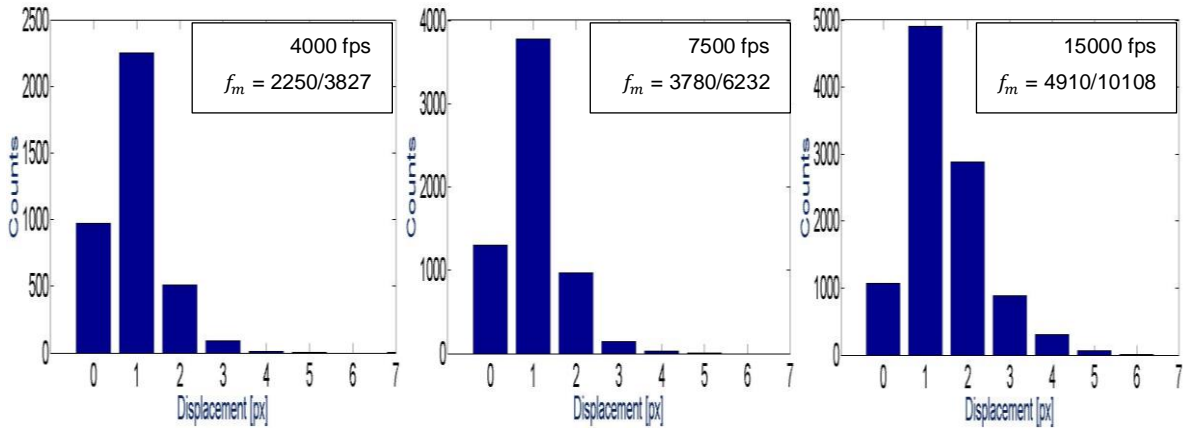
Figure 62 – (3D7 strain) Projected displacement of centroids between frames.
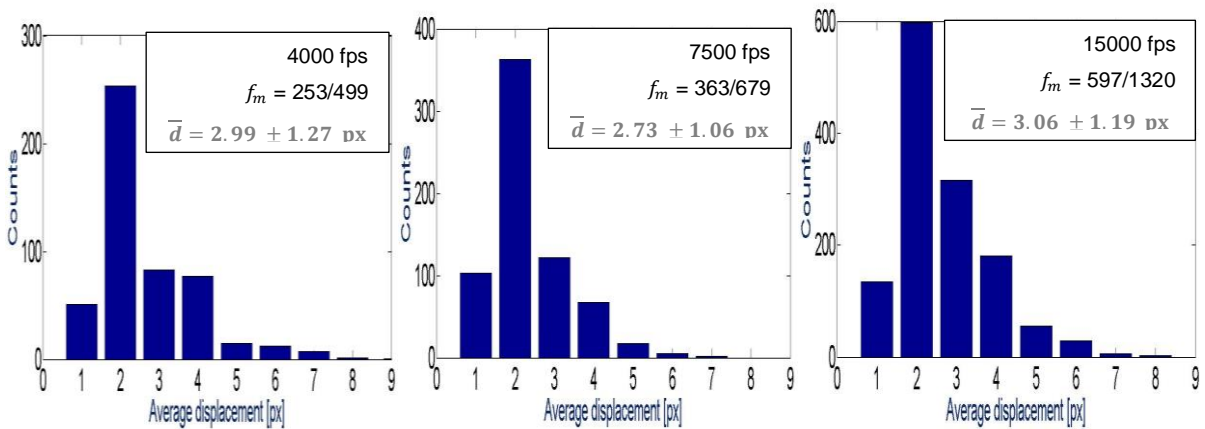
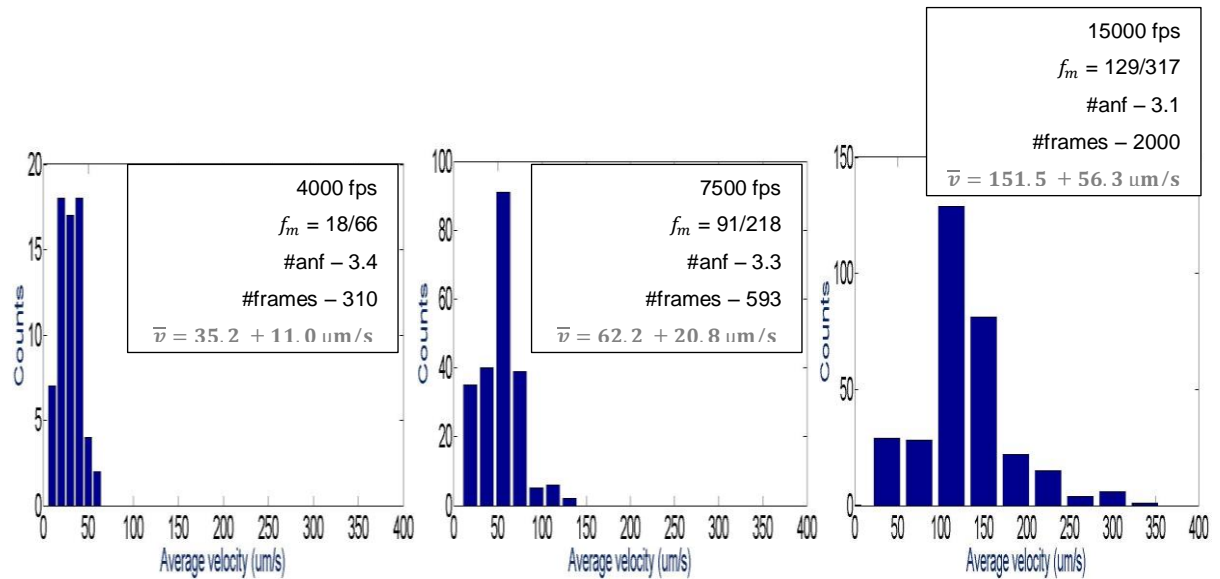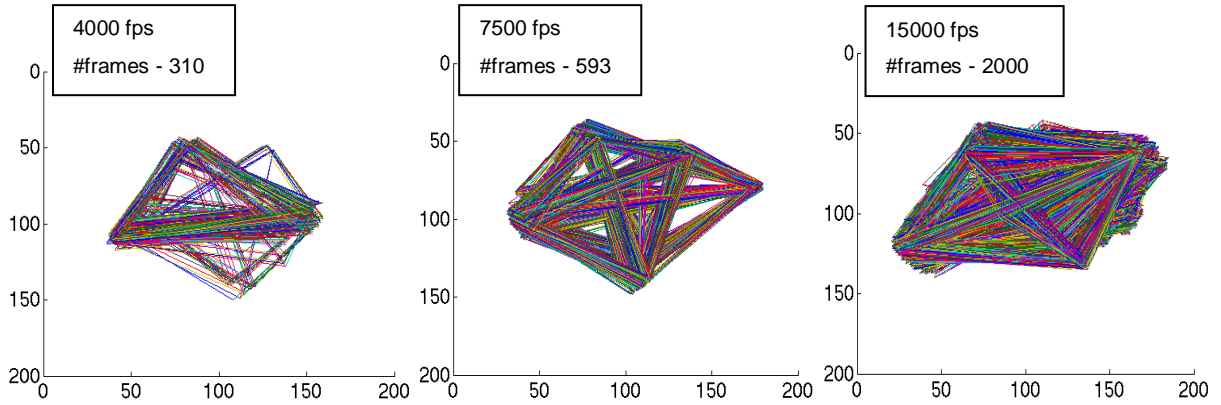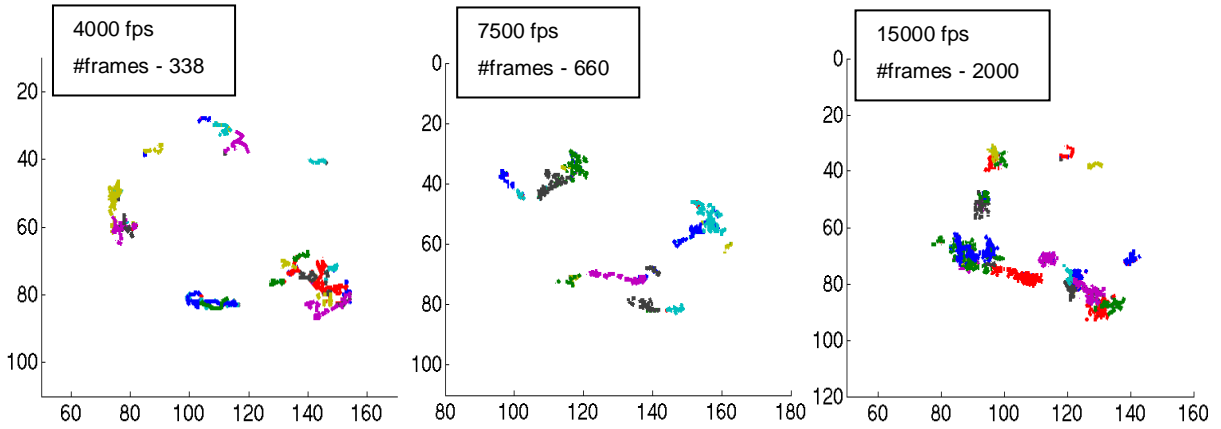**Figure 63** – (3D7 strain) Distribution of average displacement across monotonic paths.
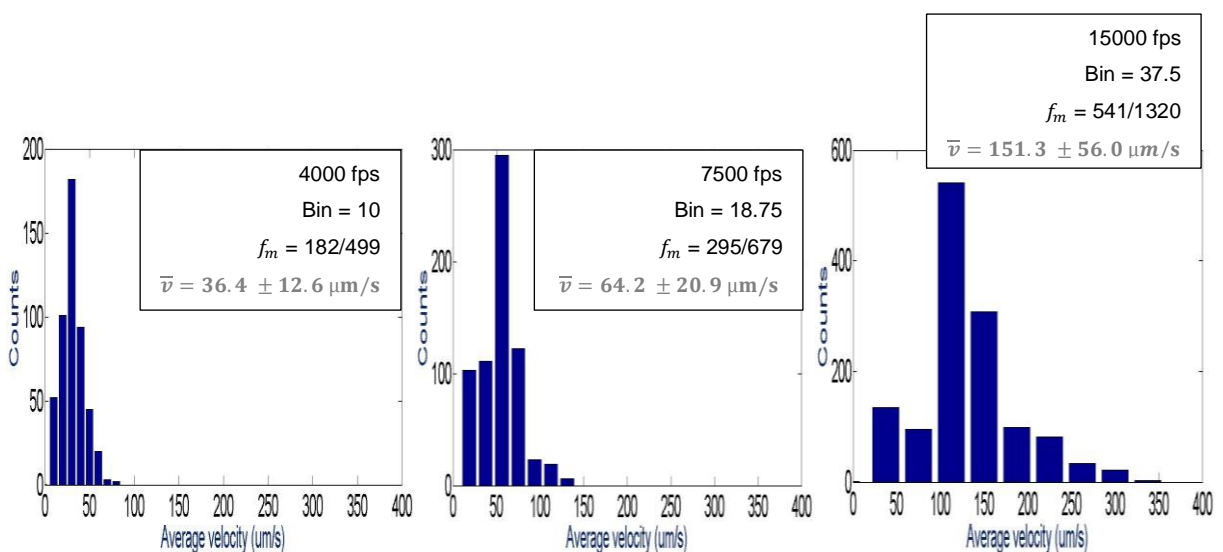
Figure 64 – (3D7 strain) Distribution of the average velocity across monotonic paths. The bin size used is proportional to the frame rate to normalize the effect of this variable.

5.2.10. Global distributions for the Dd2 strain

Figure 65 to 67 present the global results of the analyses for the Dd2 strain and a summary is presented in tables 3 and 4.
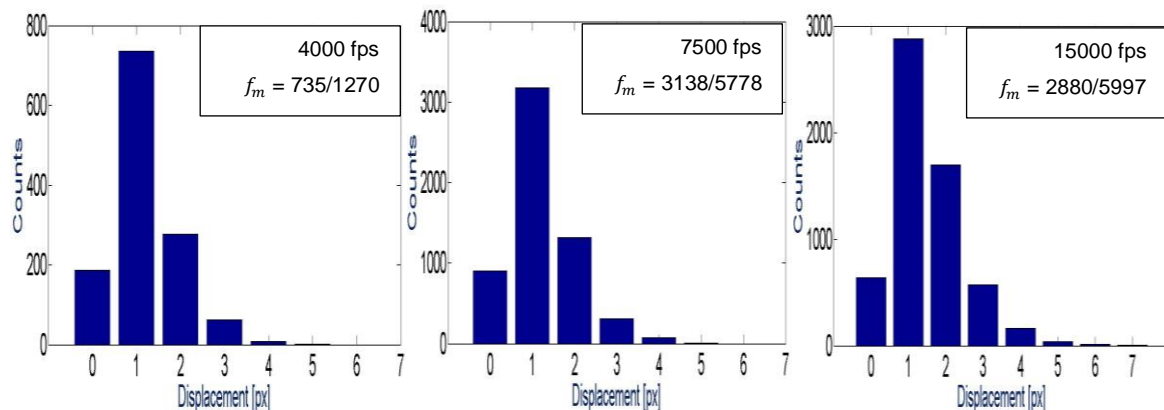
Figure 65 – (Dd2 strain) Projected displacement of centroids between frame
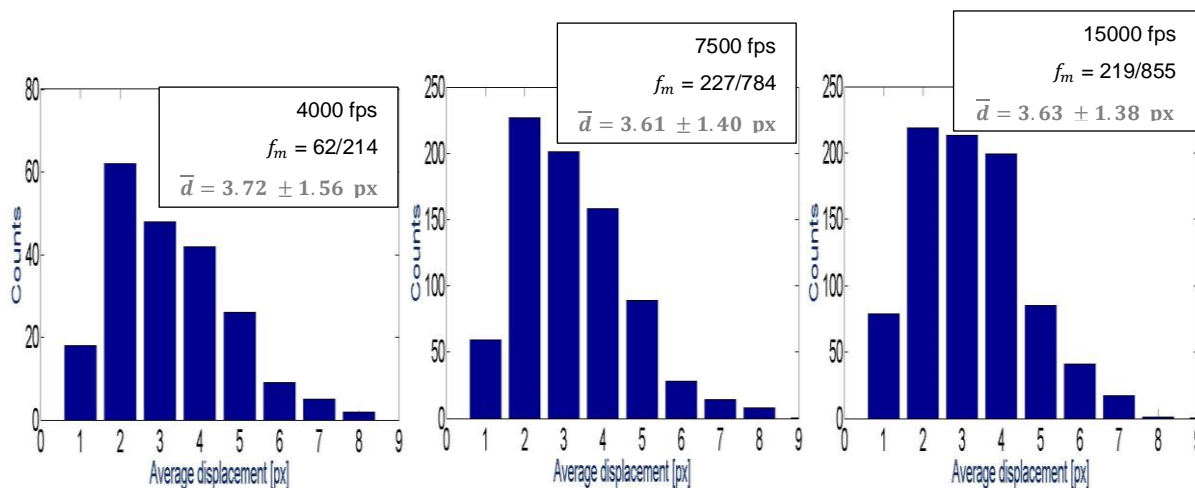
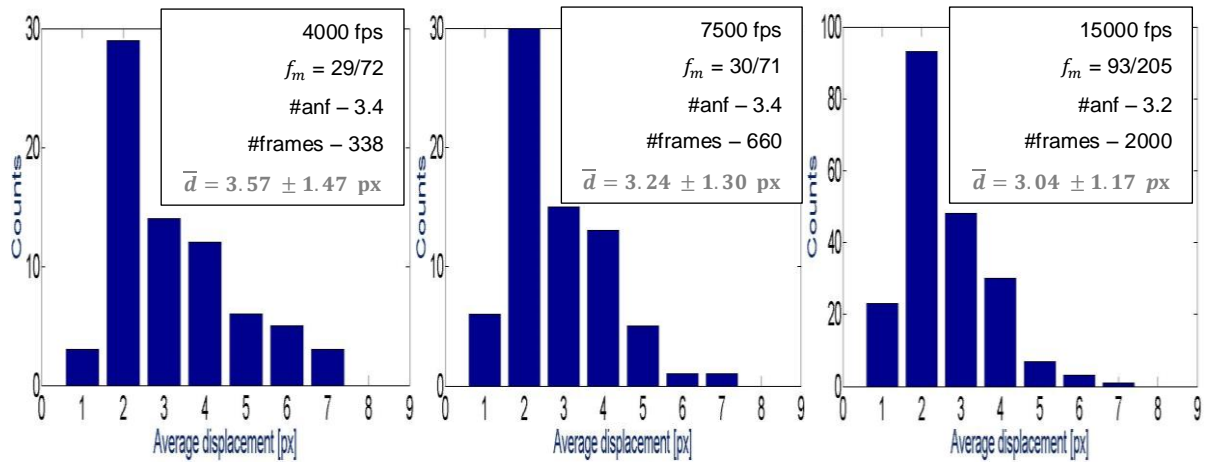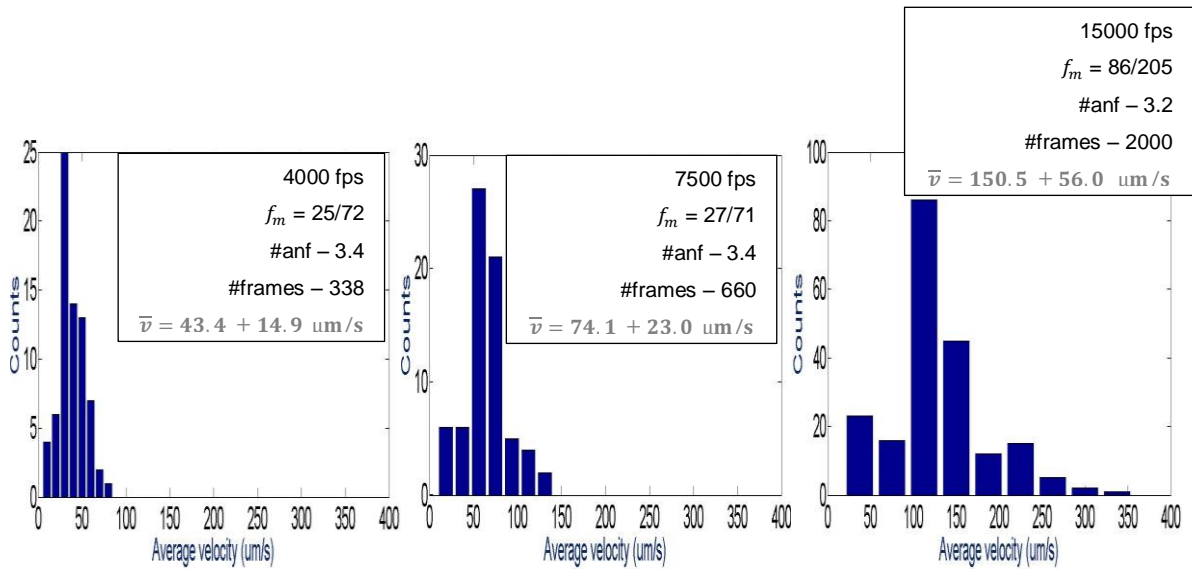**Figure 66** – (Dd2 strain) Distribution of average displacement across monotonic paths.
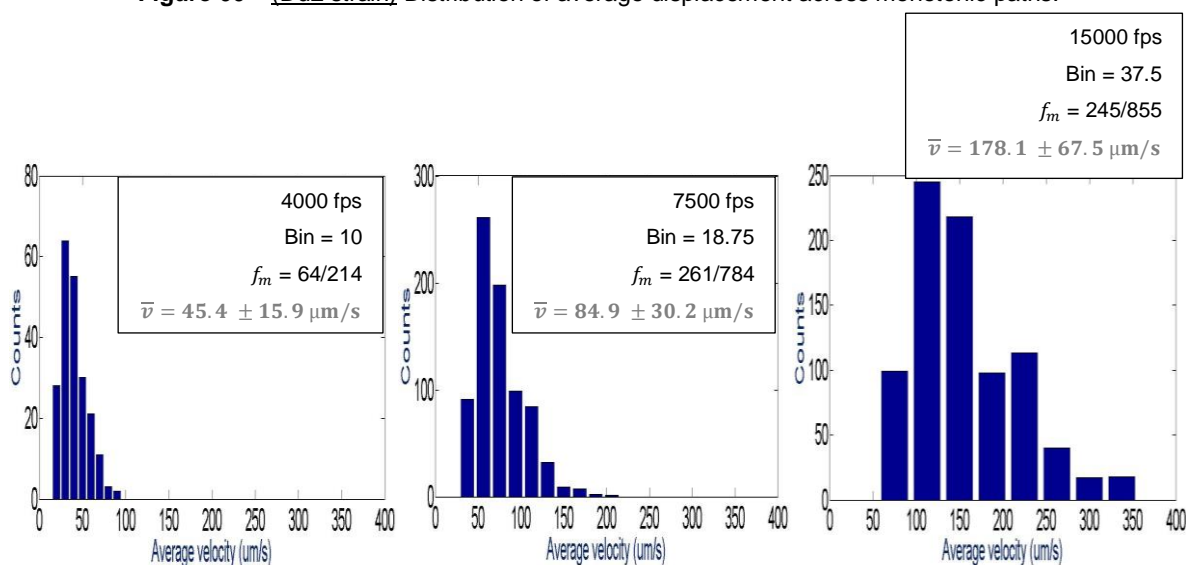
Figure 67 – (Dd2 strain) Distribution of the average velocity across monotonic paths. The bin size used is proportional to the frame rate to normalize the effect of this variable.

In the graphs representing the displacement of the centroids over time (Figures 20, 27, 32, 37, 42, 47, 52 and 57) each color corresponds to a tracked particle. The degree of overlapping suggests that multiple paths have been assigned to the same particle. This originated from the 3-dimensional nature of the movement and the limited depth of field of the observations: whenever a given particle vanished from the field of view the analysis of the path was terminated and any centroid appearing in nearby regions in the following frames of the sequence was assigned to a new path due to uncertainty.

Figures 21 and 22 demonstrate that the path of each particle shows repeated segments and that most vectors correspond to displacements of 1 pixel (see also the histograms in Figures 23, 28, 33, 38, 43, 48, 53 and 58). This behavior has been observed for all acquisitions carried out at 4000, 7500 and 15000 fps and suggests that noise is strongly affecting the results. A similar behavior was observed for the average displacements across monotonic paths: typically 3 pixels for all acquisitions carried out at 4000, 7500 and 15000 fps (see histograms in Figures 24, 29, 34, 39, 44, 49, 54 and 59 and the summary in table 3).

The fact that the average velocity determined from frame to frame or across monotonic paths scales with the frame rate (see Figures 64 and 67 and table 4) attests for the strong influence of noise in these results. The noise is probably originating from contrast variations in the spots that through filtering and segmentation resulted in random translations of the centroids used to establish the particles' paths.

Strain / frame rate	4000 fps	7500 fps	15000 fps
3D7 **Pixel: 10 nm**	2.99 ± 1.27	2.73 ± 1.06	3.06 ± 1.19
Dd2 **Pixel: 12 nm**	3.72 ± 1.56	3.61 ± 1.40	3.63 ± 1.38

Table 3 – Summary of the average displacement (in pixels) across monotonic paths for 4000 fps, 7500 fps and 15000 fps (3D7 and Dd2 strains).

Strain / frame rate	4000 fps	7500 fps	15000 fps
3D7 **Pixel: 10 nm**	36.4 ± 12.6	64.2 ± 20.9	151.3 ± 56.0
Dd2 **Pixel: 12 nm**	45.4 ± 15.9	84.9 ± 30.2	178.1 ± 67.5

Table 4 – Average velocity (in microns per second) across monotonic paths of centroids for 4000 fps, 7500 fps and 15000 fps (3D7 and Dd2 strains).

The evolution of the mutiibody configuration of the centroids in each frame, represented in the form of graphs (see Figures 26, 31, 36, 41, 46, 51, 56 and 61), shows that over the periods covered by the acquisitions the particles did not change their relative positions. This behavior, observed at 4000, 7500 and 15000 fps, is not consistent with the observations performed at lower frame rates, which suggests that at the highest frame rates the acquisition times may have been too short for a correct sampling of the movement.

In order to further investigate whether any information on movement of the particles could be retrieved from the centroids displacement in the sequences acquired at 4000, 7500 and 15000 fps, additional analyses have been carried out:

A. Determination of the maximum displacement between any pair of points of a particle path (see Figure 9 (c)). Figure 68 shows the results from this analysis and the corresponding average velocity is summarized in Table 5.

B. Determination of the maximum displacement between any pair of points in sets of paths assumed to correspond to the same particle (as indicated in Figures 69 to 73). The average velocity resulting from this analysis is summarized in Table 6.
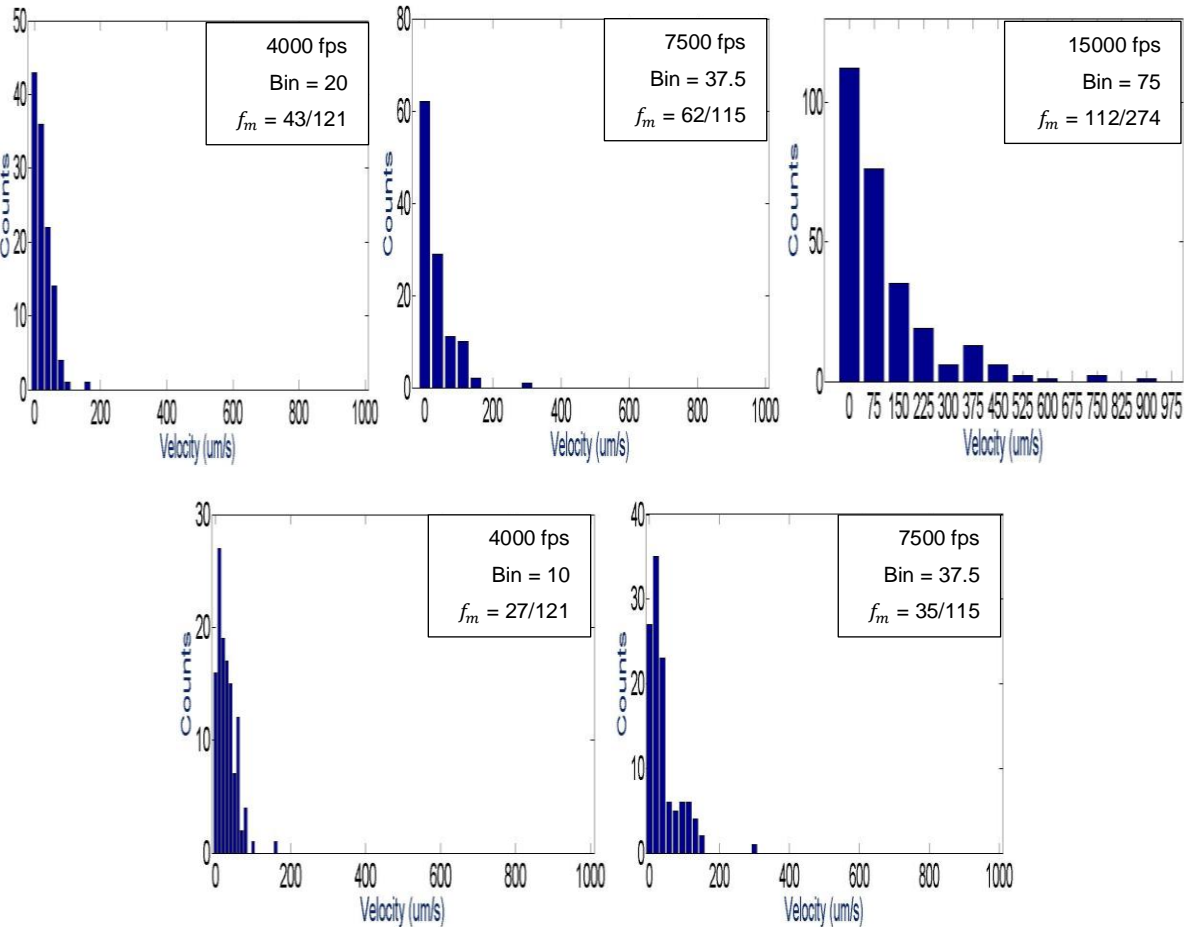
Figure 68 – Distribution of the velocity corresponding to the maximum displacements of each tracked particle. The bin size used is proportional to the frame rate to normalize the effect of this variable.

Variable / frame rate	4000 fps Pixel: 10 nm	7500 fps Pixel: 10 nm	15000 fps Pixel: 10 nm
Displacement (µm)	0.074 ± 0.009	0.080 ± 0.011	0.072 ± 0.008
#frames	10.92 ± 9.93	12.76 ± 5.83	16.89 ± 6.26
Velocity (µm/s)	34.06 ± 13.61	49.05 ± 16.26	143.42 ± 149.27

Table 5 – Average velocity and average displacement of a particle with respective standard deviations determined from the maximum displacements of each individual path.
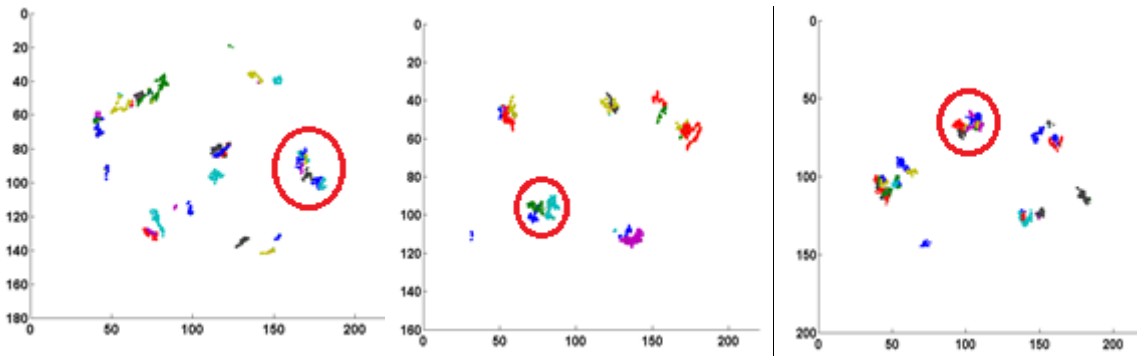
Figure 69 - Distribution of the velocity of the maximum displacements of sets of paths indicated with a red circle at 4000, 7500 and 15000 respectively (Cell 3 – 3D7 starin).
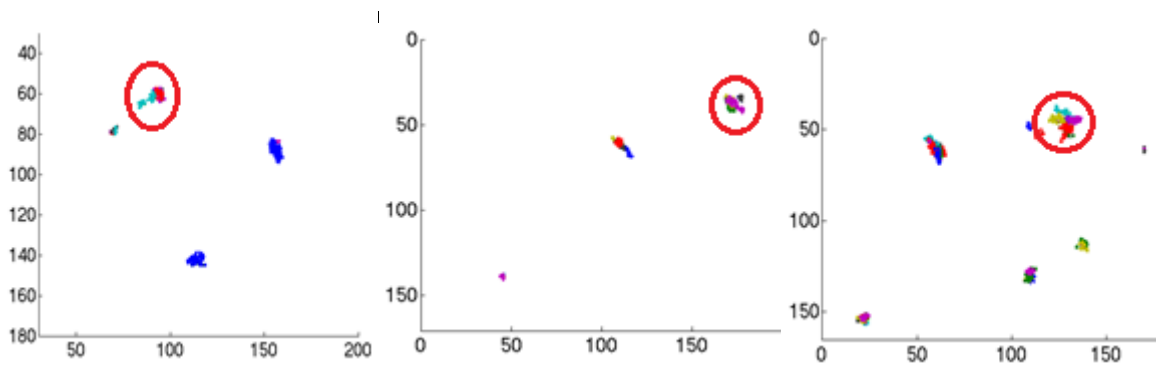
Figure 70 - Distribution of the velocity of the maximum displacements of sets of paths indicated with a red circle at 4000, 7500 and 15000 respectively (Cell 4 – 4000, 7500 and 15000 fps 3D7 strain).
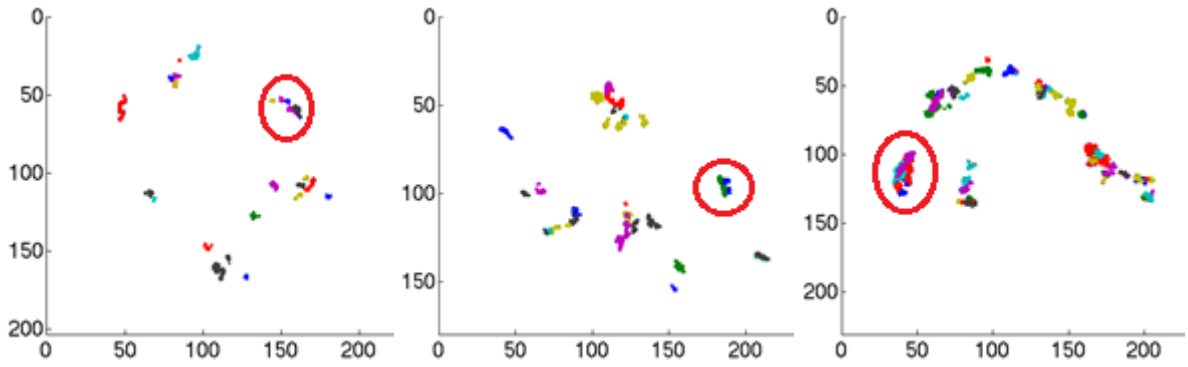
Figure 71 – Sets of paths selected for the determination of the maximum displacement of each particle (red circle) at 4000, 7500 and 15000 (Cell 5 – 3D7 strain).
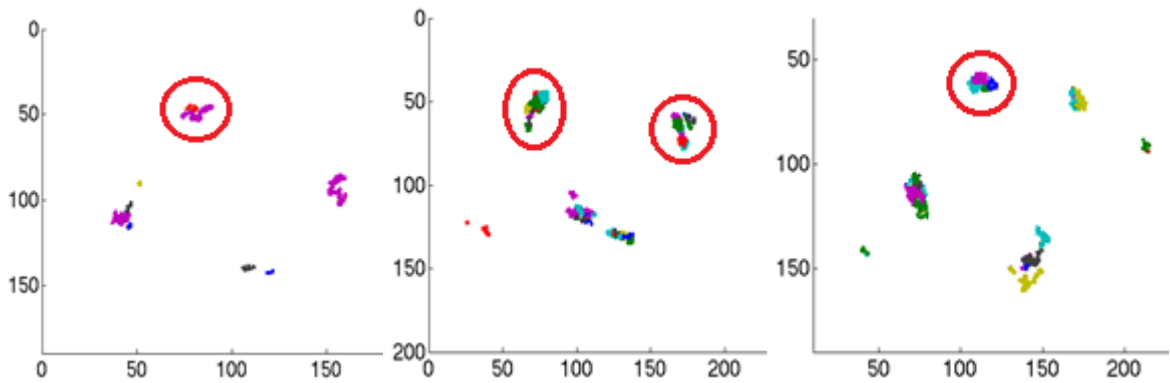
Figure 72 - Sets of paths selected for the determination of the maximum displacement of each particle (red circle) at 4000, 7500 and 15000 (Cell 6 – 3D7 strain).
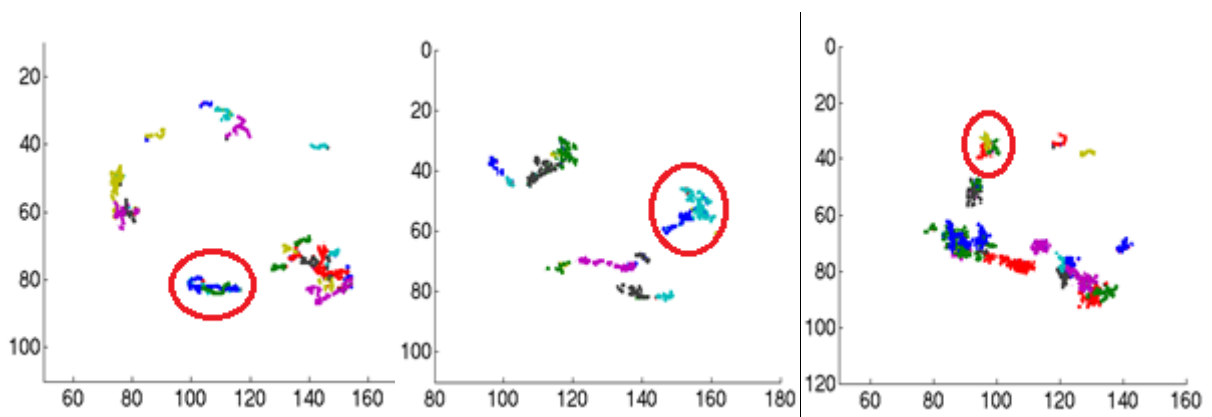
Figure 73 - Sets of paths selected for the determination of the maximum displacement of each particle (red circle) at 4000, 7500 and 15000 (Cell 7 – 3D7 strain).

Variable / frame rate	4000 fps Pixel: 10 nm	7500 fps Pixel: 10 nm	15000 fps Pixel: 10 nm
Displacement (µm)	0.200 ± 0.041	0.211 ± 0.066	0.237 ± 0.077
#frames	130.20 ± 99.75	194.00± 135.78	222.33 ± 260.83
Velocity (µm/s)	10.96 ± 9.30	14.49 ± 15.15	29.96 ± 24.34

Table 6 – Average velocity and average displacement of a particle with respective standard deviations determined from the maximum displacements in sets assumed to correspond to the same particle (indicated in Figures 69 to 73).

Although the velocity values in tables 5 and 6 are varying with the acquisition rate, the fact that for 4000 and 7500 fps they do not scale with the frame rate suggests that the influence of noise is lower than is the previous analyses. However, the high standard deviation values indicate a low precision and these results may not reflect the true characteristics of the hemozoin crystals' movement.

5.2.11. Re-analysis of frames acquired with the Mega Speed MS70K Camera.

Since the values of velocity retrieved from the centroid positions in sequences acquired at 4000, 7500 and 15000 fps have low precision, spots have also been visually tracked in the images acquired at 2128 fps with the Mega Speed MS70K Camera. For comparison, this analysis has also been performed for sequences acquired at 4000 fps with the FastCam Camera. The approach could not be carried out for the sequences acquired at 7500 or 15000 fps due to intense flickering and reduced acquisition times which made difficult tracking individual spots.

In total, 51 spots in the digestive vacuole of 3 different parasites have been tracked at 2128 fps and 21 spots in the digestive vacuole of 3 different parasites have been tracked at 4000 fps, both for the 3D7 strain. The results from this analysis are summarized in Table 7.

Variable/frame rate	2128 fps pixel: 50 nm	4000 fps pixel: 50 nm
Displacement (µm)	0.236 ± 0.090	0.190 ± 0.083
#frames	10.9 ± 2.5	12.6 ± 4.0
Velocity (µm/s)	52.5 ± 21.3	64.7 ± 25.2

Table 7 – Average values with respective standard deviations.

The fact that the velocity is not scaling with the frame rate and the lower standard deviations indicate that this analysis is more robust than the previous ones. The projected velocity of the hemozoin particles is close to 60 µm/s.

5.2.12. Temperature effect

In general, after exposure to febrile temperatures (40 °C or 41 °C for 1h) the movement of the crystals ceased. The loss of movement of hemozoin crystals can be considered one of the first indicators of an adverse response of the parasite to external stimuli, before distinct morphological changes occur [10]. After the heat treatment at 41 °C virtually all parasites exhibited immobile hemozoin crystals, while after the heat treatment at 40 °C some parasites still presented moving crystals. Therefore, contrarily to what has been stated in the literature [10], the motion of hemozoin is not Brownian in nature since the velocity does not increase with temperature and the crystals do not move in dead parasites. The fact that for the parasites exposed at 40 °C some particles resumed motion after 1 hour at room temperature is noteworthy. A quantitative characterization of the effect of febrile temperatures requires the development of an experimental protocol for image acquisition suitable to analyze the motion of the hemozoin crystals with higher accuracy and precision.

6. Conclusions

The results obtained from real-time microscopy and their analysis enable to infer that:

- The projected movement, although irregular, is compatible with a reciprocating nature and may be associated with rotation;
- The average (projected) translation velocity measured at 2128 fps is 52.5 ± 21.3 µm/s while the value obtained from measurements at 4000 fps is 64.7 ± 25.2 µm/s.
- The average free path of each particle was 0.236 ± 0.090 µm for the measurements carried out at 2128 fps and 0.190 ± 0.083 for the measurements carried out at 4000 fps.
- The crystal rotation halts after exposure to 41 °C for 1 h. After exposure at 40 °C for 1 h most crystal movement stops, however, partial resuming has been observed after 1 h at room temperature.
- The crystal movement observed has not a Brownian nature as it does not increase with temperature and the crystals do not move in dead parasites.

The dynamic behavior observed is expected to be associated with a relatively high driving force and to involve significant energy consumption. One hypothesis that remains to be proven is that it represents the means for an efficient collection of the crystallizing units.

7. Future work

As future work I suggest the acquisition of frames at rates between 2000 and 4000 fps using a camera with high resolution in order to visualize the particles' movement and follow their path with lower noise.

The fact that the particles' movement is dampen with exposure to fever and can partially resumed after fever exposure shows that the effect of temperature is not well understood and that the phenomenon demands a deeper investigation. In addition to the effect of drugs, the effect of electrical and magnetic fields on the movement of the paramagnetic hemozoin crystals is also worth studying.

A precise characterization of the hemozoin crystals' movement is necessary to cast new light on the driving forces behind this dynamic behavior and this approach is expected to pave the way for novel therapies and diagnostic tools.

8. References

[1] Newton C, Krishna S, Severe Falciparum Malaria in Children: Current Understanding of Pathophysiology and Supportive Treatment, Pharmacology & Therapeutics, Volume 79, Issue 1, July 1998, Pages 1–53;

[2] Crawley J, Nahlen B, Prevention and treatment of malaria in young African children, Seminars in Pediatric Infectious Diseases, Volume 15, Issue 3, July 2004, Pages 169–180;

[3] Santos-Magalhães N S, Mosqueira V C F, Nanotechnology applied to the treatment of malaria, Advanced Drug Delivery Reviews, Volume 62, Issues 4–5, 18 March 2010, Pages 560–575;

[4] Jerrard D A, Broder J S, Hanna J R, Colletti J E, Grundmann K A, Geroff A J, Mattu A, Malaria: a rising incidence in the United States, The Journal of Emergency Medicine, Volume 23, Issue 1, July 2002, Pages 23–33;

[5] Wykes M N, Horne-Debets J, Dendritic cells: The Trojan horse of malaria?, International Journal for Parasitology, Volume 42, Issue 6, 15 May 2012, Pages 583–587;

[6] Goldberg DE, A F Slater, A Cerami, G B Henderson. Hemoglobin degradation in the malaria parasite Plasmodium falciparum: an ordered process in a unique organelle. Proc Natl Acad Sci U S A. 1990 April; 87(8): 2931–2935;

[7] Butykai, A. et al. Malaria pigment crystals as magnetic micro-rotors: key for high-sensitivity diagnosis. Sci. Rep. 3, 1431; DOI:10.1038/srep01431 (2013);

[8] Biagini GA, Bray PG, Spiller DG, White MR, Ward SA. The digestive food vacuole of the malaria parasite is a dynamic intracellular Ca2+ store. J Biol Chem. 2003 Jul 25;278(30):27910-5. Epub 2003 May 8. PubMed PMID: 12740366;

[9] Carvalho PA, Diez-Silva M, Chen H, Dao M, Suresh S. Cytoadherence of erythrocytes invaded by Plasmodium falciparum: quantitative contact-probing of a human malaria receptor. Acta Biomater. 2013 May;9(5):6349-59.

[10] Sachanonta N, Chotivanich K, Chaisri U, Turner GD, Ferguson DJ, Day NP, Pongponratn E. Ultrastructural and real-time microscopic changes in P. falciparum-infected red blood cells following treatment with antimalarial drugs. Ultrastruct Pathol. 2011 Oct;35(5):214-25;

[11] Effects of antimalarial drugs on movement of Plasmodium falciparum, http://www.ncbi.nlm.nih.gov/pubmed/23082547

[12] http://www.who.int/mediacentre/factsheets/fs094/en/

[13] Winzeler EA, Malaria research in the post-genomic era, Nature 455 (2008) 751-756

[14] John E. Hyde, Drug-resistant malaria - an insight, FEBS Journal 274 (2007)

[15] The Lancet Infectious Diseases, Volume 13, Issue 2, Pages 114 - 115, February 2013

[16] Tilley et at. The Plasmodium falciparum-infected red blood cell, Int. J. Biochem Cell Biology 43 (2011) 839

[17] http://www.jn.pt/PaginaInicial/Sociedade/Interior.aspx?content_id=2066672

[18]   http://www.publico.pt/ciencia/noticia/portugueses-estao-a-desenvolver-uma-vacina-contra-a-malaria-1613253#/0

[19] http://www.cplab.com/index.htm

[20] http://www.photron.com/?cmd=product_general&product_id=6

[21] http://www.thelancet.com/journals/laninf/article/PIIS1473-3099%2812%2970349-3/fulltext

[22] Rosario V. Cloning of naturally occurring mixed infections of malaria parasites. Science. 1981 May 29;212(4498):1037-8. PubMed PMID: 7015505.

[23] http://micro.magnet.fsu.edu/primer/anatomy/immersion.html

[24] http://micro.magnet.fsu.edu/primer/anatomy/focusdepth.html

[25] Trager W, Jensen JB. Human malaria parasites in continuous culture. Science. 1976 Aug 20;193(4254):673-5.

[26] Lambros C, Vanderberg JP. Synchronization of Plasmodium falciparum erythrocytic stages in culture. J Parasitol. 1979 Jun;65(3):418-20.

[27] Esposito A, Tiffert T, Mauritz JMA, Schlachter S, Bannister LH, et al. (2008) FRET Imaging of Hemoglobin Concentration in *Plasmodium falciparum*-Infected Red Cells. PLoS ONE 3(11): e3780. doi:10.1371/journal.pone.0003780

[28] Johann, L., Lanfranchi, D. A., Davioud-Charvet, E., & Elhabiri, M. (2012). A Physico-Biochemical Study on Potential Redox-Cyclers as Antimalarial and Antischistosomal Drugs. *Current Pharmaceutical Design*, *18*(24), 3539–3566.

[29] Carvalho P.A., L. Coelho, R.C. Martins and F. Nogueira. Differences between synthetic ß-haematin and native hemozoin crystals. Microscopy and Microanalysis. 2013 19 (Suppl. 4), pp 49-50. doi:10.1017/S143192761300086X. IF 2.992

[30] http://www.vtnews.vt.edu/articles/2008/05/2008-322.html

[31] Goldberg, Daniel E; .Complex nature of malaria parasite hemoglobin degradation, vol. 110 no. 14, 5283-5284, 2013;

[32] Kapishnikov, Sergey et al; Oriented nucleation of hemozoin at the digestive vacuole membrane in *Plasmodium falciparum,* vol. 109 no. 28, 11188-11193, 2012

Annex 1 – Scripts employed in the calculations

```
%Image segmentation (ImageJ)


name = getTitle();
makeRectangle(261, 259, 70, 70);
run("Crop");
run("Bandpass Filter...", "filter_large=40 filter_small=15
suppress=Vertical tolerance=0 autoscale saturate");
run("Find Maxima...", "noise=10 output=[Maxima Within Tolerance] exclude
light");
run("Invert");
saveAs("Tiff",
"/Users/patriciacarvalho/Dropbox/rotors/Graphs/Graph_cell15_15000fps/tratad
as/"+name+".tif");
close();
```

```
%Determination of particle centroids(ImageJ)


name = getTitle();
run("Find Maxima...", "noise=10 output=List exclude light");
saveAs("Results",
"/Users/patriciacarvalho/Dropbox/rotors/Graphs/Graph_cell15_4000fps/"+name+
".txt")
close();
```

```matlab
% Identification of x,y coordinates of particles center of mass in each
frame (MATLAB)


%Select data, first frame and number of frames
filme='TROPHO_37C_10FEV_7500_C001H001S00010'; %Common string in the name of
all frames
ini=601; %First frame
nFrame=58; %Number of frames in the sequence

irow=124; %(y1 do imageJ)
icol=31; %(x1 do imageJ)
endrow=153; %(y2 do imageJ)
endcol=59; %(x2 do imageJ)
local=zeros(nFrame+1,2);
desloc=zeros(nFrame,3);

for i=ini:nFrame+ini
    Im  = imread([filme,num2str(i,'%05u'),'.tif']);
    [row,column] = find(Im(irow:endrow,icol:endcol)==255,1,'first');
    local(i+1-ini,1)=icol+column-1;
    local(i+1-ini,2)=irow+row-1;
    if i>=ini+1
        desloc(i-ini,1)=local(i+1-ini,1)-local(i-ini,1);
        desloc(i-ini,2)=local(i+1-ini,2)-local(i-ini,2);
        desloc(i-ini,3)=sqrt(desloc(i-ini,1)^2+desloc(i-ini,2)^2);
    end
end

bin=[0:5];
figure(), bar(bin,histc(desloc(:,3),bin))
```

```matlab
%Tracking of particle movement (MATLAB)



load('cell8_15000fps.mat') %Load the .mat including x,y positions
A =  cell8_15000fps; %matrix consisting of concatenated (x,y) columns (2
for each particle), padded with zeros at bottom rows)

%prepare matrix of results
[rows, columns] = size(A);
figure ();
axis ij;
set(findall(gcf,'type','axes'),'fontSize',24,'fontWeight','bold');
set(gcf,'DefaultLineLineWidth',1.0);
hold on

for n = 1:2:columns-1
        x = A(:,n);
        row = find(x==0, 1);
        x = A(1:row-1,n);
        y = A(1:row-1,n+1);
        u = zeros(row-1,1);
        v = zeros(row-1,1);

        for m = 1:row-2;
            u(m)=x(m+1)-x(m);
            v(m)=y(m+1)-y(m);
            quiver(x,y,u,v,0,'ShowArrowHead','on');
end
end
```

```matlab
%Overlapping frame graphs (MATLAB)



%Select data, first frame and number of frames
name        ='TROPHO_37C_7FEV_7500_C001H001S00010'; %Common string in the
name of all frames
ini         =1; %First frame
nFrame      =999; %Number of frames in the sequence

figure ();%Open an image
axis([0 315 0 222]); %Image with these dimensions
set(findall(gcf,'type','axes'),'fontSize',24,'fontWeight','bold');
axis ij;
hold on

for i = ini:nFrame+ini %x,y,x,y,x,y,...
    fileID = fopen([name,num2str(i,'%05u'),'.tif.tif.tif.txt'],'r');
    fgets(fileID);
    A = fscanf(fileID,'%d',[3 inf]);
    fclose(fileID);
    A=A';
    [rows columns] = size(A);
    for n=1:rows
        for m=1:rows-1
        quiver(A(n,2),A(n,3),A(m+1,2)-A(n,2),A(m+1,3)-
A(n,3),0,'ShowArrowHead','off');
        hold on
        end
    end
end
```

```matlab
%Maximum dislocation of each particle and minorant of velocity (MATLAB)


%Select data, frame rate and pixel size
A  =  filme12_4000fps; %matrix consisting of concatenated (x,y) columns (2
for each particle), padded with zeros at bottom rows)
fps =4000; %frame rate
pixel = 0.010; %conversion from pixel to nm

%prepare matrix of results
[rows, columns] = size(A);
[speed_particles] = []; %column vector to be filled with speed values
determined from max displacements


%displacements bewteen frames in combinations of 2: selecting max value(s):
%calculating the correspondig speed
for m = 1:2:columns-1 %x,y,x,y,x,y,...
        x = A(:,m);
        row_zero = find(x==0, 1); %the original (x,y) columns are unevenly
padded with zeros at the bottom
        x = A(1:row_zero-1,m); %x vector of particle m
        y = A(1:row_zero-1,m+1); %y vector of particle m
        displacement = 0; % inicial displacement for each particle
        for n = 1:1:row_zero-2;
            for s = n+1:1:row_zero-1; %combining the m (x,y) values with
the s (x,y) values
                u =x(s)-x(n);
                v =y(s)-y(n);
                new_displacement = sqrt(u^2+v^2);
                if new_displacement > displacement;
                   displacement = new_displacement;
                   frame_dif = s-n;
                   speed = displacement*pixel*fps/frame_dif;
                   speed_max = [m,n,s,displacement,speed];
                else
                    if new_displacement == displacement; %in case there are
more than one max values
                        new_frame_dif = s-n;
                        if new_frame_dif < frame_dif; %aiming for the one
corresponding the smalest frame difference
                            frame_dif = new_frame_dif;
                            speed = displacement*pixel*fps/frame_dif;
                            speed_max = [m,n,s,displacement,speed];
%column, inicialframe, finalframe, displacement max, corresponding speed
                        end
                    end
                end
            end

        end
        [speed_particles] = [speed_particles;speed_max]; %new line added
per particle
end
speed_max = max(speed_particles(:,5));
average = mean(speed_particles(:,5));
```